

The GAPS Programme with HARPS-N at TNG*

VIII: Observations of the Rossiter-McLaughlin effect and characterisation of the transiting planetary systems HAT-P-36 and WASP-11/HAT-P-10

L. Mancini^{1,2}, M. Esposito^{3,4}, E. Covino⁵, G. Raia⁵, J. Southworth⁶, J. Tregloan-Reed⁷, K. Biazzo⁸, A. Bonomo², S. Desidera⁹, A. F. Lanza⁸, G. Maciejewski¹⁰, E. Poretti¹¹, A. Sozzetti², F. Borsa¹¹, I. Bruni¹², S. Ciceri¹, R. Claudi⁹, R. Cosentino¹³, R. Gratton⁹, A. F. Martinez Fiorenzano¹³, G. Lodato¹⁴, V. Lorenzi¹³, F. Marzari^{9,13}, S. Murabito^{3,4}, L. Affer¹⁵, A. Bignamini¹⁶, L. R. Bedin⁹, C. Boccato⁹, M. Damasso², Th. Henning¹, A. Maggio¹⁵, G. Micela¹⁵, E. Molinari^{13,17}, I. Pagano⁸, G. Piotto^{9,18}, M. Rainer¹¹, G. Scandariato⁸, R. Smareglia¹⁶, and R. Zanmar Sanchez⁸

¹ Max Planck Institute for Astronomy, Königstuhl 17, 69117 – Heidelberg, Germany
e-mail: mancini@mpia.de

² INAF – Osservatorio Astrofisico di Torino, via Osservatorio 20, 10025 – Pino Torinese, Italy

³ Instituto de Astrofísica de Canarias, C/ Vía Láctea s/n, 38205 – La Laguna, Tenerife, Spain

⁴ Dep. de Astrofísica, Universidad de La Laguna, Avda. Astrofísico F. Sánchez s/n, 38206 La Laguna, Tenerife, Spain

⁵ INAF – Osservatorio Astronomico di Capodimonte, via Moiariello 16, 80131 – Naples, Italy

⁶ Astrophysics Group, Keele University, Keele ST5 5BG, UK

⁷ NASA Ames Research Center, Moffett Field, CA 94035, USA

⁸ INAF – Osservatorio Astrofisico di Catania, via S. Sofia 78, 95123 – Catania, Italy

⁹ INAF – Osservatorio Astronomico di Padova, Vicolo dell'Osservatorio 5, 35122 – Padova, Italy

¹⁰ Centre for Astronomy, Nicolaus Copernicus University, Grudziadzka 5, 87-100 – Torun, Poland

¹¹ INAF – Osservatorio Astronomico di Brera, via E. Bianchi 46, 23807 – Merate (Lecco), Italy

¹² INAF – Osservatorio Astronomico di Bologna, Via Ranzani 1, 40127 – Bologna, Italy

¹³ Fundación Galileo Galilei - INAF, Rambla José Ana Fernández Pérez, 738712 – Breña Baja, Tenerife, Spain

¹⁴ Dipartimento di Fisica, Università di Milano, via Celoria 16, 20133 – Milano, Italy

¹⁵ INAF – Osservatorio Astronomico di Palermo, Piazza del Parlamento, 90134 – Palermo, Italy

¹⁶ INAF – Osservatorio Astronomico di Trieste, via Tiepolo 11, 34143 – Trieste, Italy

¹⁷ INAF – IASF Milano, via Bassini 15, 20133 – Milano, Italy

¹⁸ Dip. di Fisica e Astronomia Galileo Galilei, Università di Padova, Vicolo dell'Osservatorio 2, 35122 – Padova, Italy

Preprint online version: July 23, 2018

ABSTRACT

Context. Orbital obliquity is thought to be a fundamental parameter in tracing the physical mechanisms that cause the migration of giant planets from the snow line down to roughly 10^{-2} au from their host stars. We are carrying out a large programme to estimate the spin-orbit alignment of a sample of transiting planetary systems to study what the possible configurations of orbital obliquity are and whether they correlate with other stellar or planetary properties.

Aims. We determine the true and the projected obliquity of HAT-P-36 and WASP-11/HAT-P-10 systems, respectively, which are both composed of a relatively cool star (with effective temperature $T_{\text{eff}} < 6100$ K) and a hot-Jupiter planet.

Methods. Thanks to the high-resolution spectrograph HARPS-N, we observed the Rossiter-McLaughlin effect for both the systems by acquiring precise ($3 - 8 \text{ m s}^{-1}$) radial-velocity measurements during planetary transit events. We also present photometric observations comprising six light curves covering five transit events, which were obtained using three medium-class telescopes. One transit of WASP-11/HAT-P-10 was followed contemporaneously from two observatories. The three transit light curves of HAT-P-36 b show anomalies attributable to starspot complexes on the surface of the parent star, in agreement with the analysis of its spectra that indicate a moderate activity ($\log R'_{\text{HK}} = -4.65$ dex). By analysing the complete HATNet data set of HAT-P-36, we estimated the stellar rotation period by detecting a periodic photometric modulation in the light curve caused by star spots, obtaining $P_{\text{rot}} = 15.3 \pm 0.4$ days, which implies that the inclination of the stellar rotational axis with respect to the line of sight is $i_* = 65^\circ \pm 34^\circ$.

Results. We used the new spectroscopic and photometric data to revise the main physical parameters and measure the sky-projected misalignment angle of the two systems. We found $\lambda = -14^\circ \pm 18^\circ$ for HAT-P-36 and $\lambda = 7^\circ \pm 5^\circ$ for WASP-11/HAT-P-10, indicating in both cases a good spin-orbit alignment. In the case of HAT-P-36, we also measured its real obliquity, which turned out to be $\psi = 25^{+38}_{-25}$ degrees.

Key words. stars: planetary systems – stars: fundamental parameters – stars: individual: HAT-P-36 – stars: individual: WASP-11/HAT-P-10 – techniques: radial velocities – techniques: photometric

1. Introduction

Since its discovery (Mayor & Queloz 1995), hot Jupiters have challenged the community of theoretical astrophysicists to explain their existence. They are a population of gaseous giant extrasolar planets, similar to Jupiter, but revolving very close to their parent stars (between ~ 0.01 and 0.05 au), which causes them to have orbital periods of few days and high equilibrium temperatures (between ~ 400 and 2750 K)¹. According to the generally accepted theory of planet formation (we refer the reader to the review of Mordasini et al. 2014), hot Jupiters are thought to form far from their parent stars, beyond the so-called *snow line*, and then *migrate* inwards to their current positions at a later time. However, the astrophysical mechanism that regulates this migration process, as that which causes planets moving on misaligned orbits, is still a matter of debate.

Spin-orbit obliquity, ψ , that is the angle between a planet's orbital axis and its host star's spin, could be the primary tool to understand the physics behind the migration process of giant planets (e.g., Dawson 2014 and references therein). A broad distribution of ψ is expected for giant planets, whose orbits are originally large (beyond the snow line) and (being perturbed by other bodies) highly eccentric, and then become smaller and circularized by planet's tidal dissipation during close periastron passages. Instead, a much smoother migration, like the one through a proto-planetary disc, should preserve a good spin-orbit alignment and, assuming that the axis of the proto-planetary disk remains constant with time, imply a final hot-Jupiter population with $\psi \simeq 0$.

The experimental measurement of ψ for a large sample of hot Jupiters is mandatory to guide our comprehension of such planetary evolution processes in the meanders of theoretical speculations. Unfortunately, this quantity is very difficult to determine, and only a few measurements exist (e.g., Brothwell et al. 2014; Lendl et al. 2014; Lund et al. 2014). However, its sky projection, λ , is a quantity which is commonly measured for stars hosting *transiting exoplanets* through the observation of the Rossiter-McLaughlin (RM) effect with high-precision radial-velocity (RV) instruments. Such measurements have revealed a wide range of obliquities in both early- and late-type stars (e.g., Triaud et al. 2010; Albrecht et al. 2012b), including planets revolving perpendicular (e.g., Albrecht et al. 2012a) or retrograde (e.g., Anderson et al. 2010; Hébrard et al. 2011; Esposito et al. 2014) to the direction of the rotation of their parent stars. The results collected so far are not enough to provide robust statistics and more investigations are needed to infer a comprehensive picture for identifying what the most plausible hot-Jupiter migration channels are.

Within the framework of GAPS (Global Architecture of Planetary Systems), a manifold long-term observational programme, using the high-resolution spectrograph HARPS-N at the 3.58 m TNG telescope for sev-

eral semesters (Desidera et al. 2013, 2014; Damasso et al. 2015), we are carrying out a subprogramme aimed at studying the spin-orbit alignment of a large sample of known transiting extrasolar planet (TEP) systems (Covino et al. 2013). This subprogramme is supported by photometric follow-up observations of planetary-transit events of the targets in the sample list by using an array of medium-class telescopes. Monitoring new transits is useful for getting additional information, as stellar activity, and for constraining the whole set of physical parameters of the TEP systems better. When possible, photometric observations are simultaneously performed with the measurement of the RM effect, benefiting from the two-telescope observational strategy (Ciceri et al. 2013).

Here, we present the results for two TEP systems: HAT-P-36 and WASP-11/HAT-P-10.

The paper is organized as follows. In Sect. 1.1 we briefly describe the two systems, subjects of this research study. The observations and reduction procedures are treated in Sect. 2, while Sect. 3 is dedicated to the analysis of the photometric data and the refining of the orbital ephemerides; anomalies detected in the HAT-P-36 light curves are also discussed. In Sect. 4 the HARPS-N time-series data are used to determine the stellar atmospheric properties and measure the spin-orbit relative orientation of both the systems. Sect. 5 is devoted to the revision of the main physical parameters of the two planetary systems, based on the data previously presented. General empirical correlations between the orbital obliquity and various properties of TEP systems are discussed in Sect. 6. The results of this work are finally summarised in Sect. 7.

1.1. Case history

HAT-P-36, discovered by the HAT-Net survey (Bakos et al. 2012), is composed of a $V = 12.5$ mag, G5 V star (this work), similar to our Sun, and a hot Jupiter (mass $\sim 1.8 M_{\text{Jup}}$ and radius $\sim 1.3 R_{\text{Jup}}$), which revolves around its parent star in nearly 1.3 days. The only follow-up study of this system has provided a refinement of the transit ephemeris based on the photometric observation of two planetary transits performed with a 0.6 m telescope (Maciejewski et al. 2013).

The discovery of the WASP-11/HAT-P-10 TEP system was almost concurrently announced by the WASP (West et al. 2009) and HAT-Net (Bakos et al. 2009) teams. It is composed of a $V = 11.9$ mag, K3 V star (Ehrenreich & Désert 2011) (mass $\sim 0.8 M_{\odot}$ and radius $\sim 0.8 R_{\odot}$) and a Jovian planet (mass $\sim 0.5 M_{\text{Jup}}$ and radius $\sim 1 R_{\text{Jup}}$), moving on a 3.7 day circular orbit. Four additional transit observations of this target were obtained by Sada et al. (2012) in z' and J bands with a 0.5 m and 2.1 m telescope, respectively, which were used to refine the transit ephemeris and photometric parameters. In a more recent study (Wang et al. 2014), an additional four new light curves, which were obtained with a 1 m telescope, were presented and most of the physical parameters were revised, confirming the results of the two discovery papers.

2. Observation and data reduction

In this section we present new spectroscopic and photometric follow-up observations of HAT-P-36 and WASP-

* Based on observations made with (i) the Italian 3.58 m Telescopio Nazionale Galileo at the Observatory of Roque de los Muchachos, (ii) the Cassini 1.52 m telescope at the Astronomical Observatory of Bologna, (iii) the Zeiss 1.23 m telescope at the Observatory of Calar Alto, and the IAC 80 cm telescope at the Teide Observatory.

¹ Data taken from TEPcat (Transiting Extrasolar Planet Catalogue), available at www.astro.keele.ac.uk/jkt/tepcat/ (Southworth 2011).

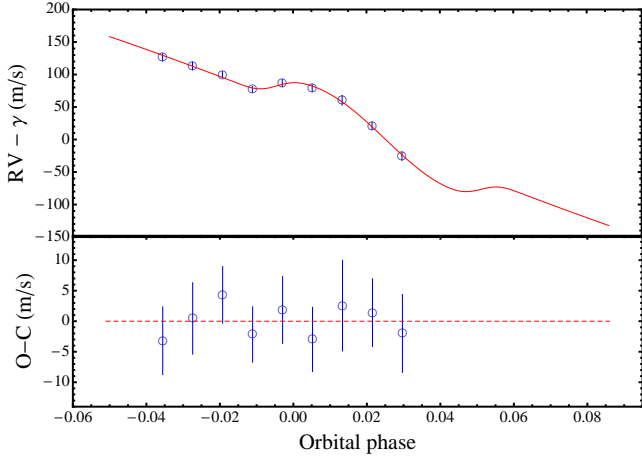


Fig. 1. Phase-folded RV data of a partial transit of HAT-P-36 b observed with HARPS-N. Superimposed is the best-fitting RV-curve model. The corresponding residuals are plotted in the lower panel. Phase 0 corresponds to the time of the planet passing the periastron.

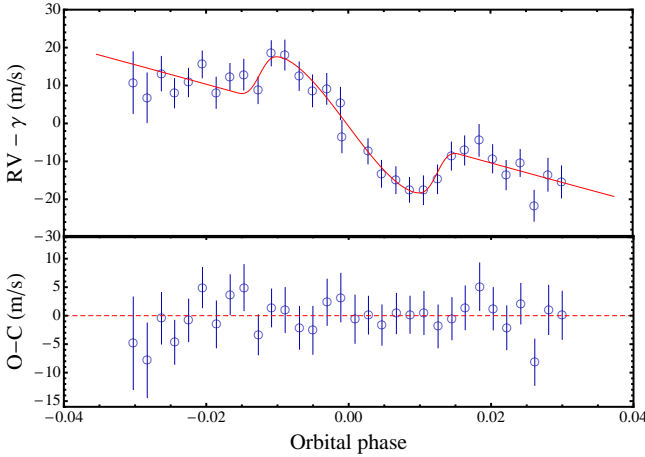


Fig. 2. Phase-folded RV data of a complete transit of WASP-11 b observed with HARPS-N. Superimposed is the best-fitting RV-curve model. The corresponding residuals are plotted in the lower panel.

11/HAT-P-10. For both the planetary systems, the RM effect was measured for the first time and three complete transit light curves were acquired.

2.1. HARPS-N spectroscopic observations

Spectroscopic observations of the two targets were performed using the HARPS-N (High Accuracy Radial velocity Planet Searcher-North; Cosentino et al. 2012) spectrograph at the 3.58m TNG, in the framework of the above-mentioned GAPS programme.

A sequence of spectra of HAT-P-36 was acquired on the night 2013 February 21 during a transit event of its planet, with an exposure time of 900sec. Unfortunately, because of high humidity, the observations were stopped before the transit was over and thus only nine measurements were obtained that cover a bit more than the first half of the transit.

Table 1. HARPS-N RV measurements of HAT-P-36 and WASP-11/HAT-P-10.

BJD(TDB)	RV (m s ⁻¹)	Error (m s ⁻¹)
HAT-P-36:		
2 456 345.583549	-16200.7	5.5
2 456 345.594369	-16213.9	5.8
2 456 345.605189	-16227.2	4.6
2 456 345.616014	-16249.9	4.6
2 456 345.626843	-16240.2	5.5
2 456 345.637659	-16247.8	5.3
2 456 345.648483	-16266.6	7.4
2 456 345.659304	-16306.0	5.5
2 456 345.670130	-16352.7	6.4
WASP-11/HAT-P-10:		
2 456 933.502525	4907.4	8.0
2 456 933.509760	4901.6	6.5
2 456 933.516999	4907.8	4.5
2 456 933.524234	4902.7	3.8
2 456 933.531469	4905.5	3.7
2 456 933.538699	4910.1	3.5
2 456 933.545929	4902.3	4.1
2 456 933.553165	4907.2	3.5
2 456 933.560400	4908.2	4.0
2 456 933.567644	4902.8	3.5
2 456 933.574884	4913.1	3.3
2 456 933.582122	4913.4	3.9
2 456 933.589366	4907.7	3.7
2 456 933.596598	4903.3	4.2
2 456 933.603834	4904.6	4.0
2 456 933.611071	4899.7	4.2
2 456 933.618316	4891.2	4.2
2 456 933.625565	4887.1	3.3
2 456 933.632809	4880.9	3.5
2 456 933.640053	4879.5	3.5
2 456 933.647298	4877.8	3.2
2 456 933.654533	4877.9	3.8
2 456 933.661763	4879.4	3.7
2 456 933.669002	4885.9	3.7
2 456 933.676238	4887.0	3.8
2 456 933.683469	4891.0	4.1
2 456 933.690700	4884.7	3.7
2 456 933.697935	4881.6	3.8
2 456 933.705166	4884.5	3.5
2 456 933.712397	4873.5	4.0
2 456 933.719632	4881.2	4.3
2 456 933.726867	4879.8	4.2

A complete spectroscopic transit of WASP-11/HAT-P-10b was recorded on 2014 October 2. A sequence of 32 spectra was obtained using an exposure time of 600sec.

The spectra were reduced using the latest version of the HARPS-N instrument Data Reduction Software pipeline. The pipeline also provides rebinned 1D spectra that we used for stellar characterization (see summary Table 8 and 9), in particular to estimate the stellar effective temperature, T_{eff} , and metal abundance [Fe/H] (see Sect. 4.1). Radial velocities were measured by applying the weighted cross-correlation function (CCF) method (Baranne et al. 1996; Pepe et al. 2002) and using a G2 and a K5 mask for HAT-P-36 and WASP-11/HAT-P-10, respectively. They are reported in Table 1 and plotted in Figs. 1 and 2, in which we can immediately note that the RM effect was successfully observed. It indicates low orbital obliquity for both the systems.

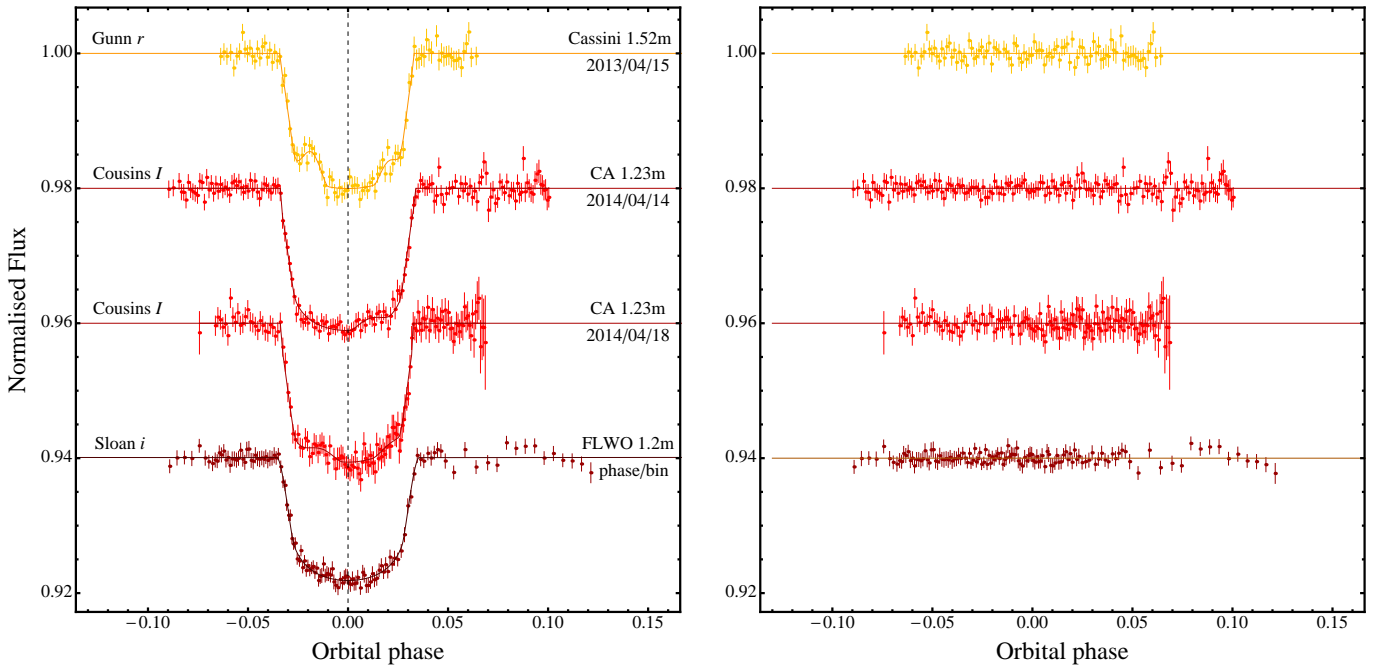


Fig. 3. Light curves of HAT-P-36 b transits compared with the best PRISM+GEMC fits. The dates, the telescopes and the filters used for each transit event are indicated. Residuals from the fits are displayed in the *right panel*. Starting from the top, the first three light curves (this work) present anomalies that we interpret as occultations of starspot complexes by the planet. The third light curve is related to the transit event successive to that of the second one. The last light curve was extracted from Bakos et al. (2012) and reported here for comparison. Here phase 0 corresponds to the mid-time of the transit.

2.2. Photometric follow-up observations of HAT-P-36

One transit of HAT-P-36 b was observed on April 2013 through a Gunn-*r* filter with the Bologna Faint Object Spectrograph & Camera (BFOSC) imager mounted on the 1.52 m Cassini Telescope at the Astronomical Observatory of Bologna in Loiano, Italy. The CCD was used unbinned, giving a plate scale of $0.58 \text{ arcsec pixel}^{-1}$, for a total FOV of $13 \text{ arcmin} \times 12.6 \text{ arcmin}$. Two successive transits were observed on April 2014 by using the Zeiss 1.23 m telescope at the German-Spanish Astronomical Center at Calar Alto, Spain. This telescope is equipped with the DLR-MKIII camera, which has 4000×4000 pixels, a plate scale of $0.32 \text{ arcsec pixel}^{-1}$ and a FOV of $21.5 \text{ arcmin} \times 21.5 \text{ arcmin}$. The observations were performed remotely, a Cousins-*I* filter was adopted and the CCD was used unbinned, too. Details of the observations are reported in Table 2. As in previous uses of the two telescopes (e.g. Mancini et al. 2013a), the *defocussing* technique was adopted in all the observations to improve the quality of the photometric data remarkably. Telescopes were also autoguided.

The data were reduced with a modified version of the DEFOT pipeline, written in IDL², which is exhaustively described in Southworth et al. (2014). In brief, we created master calibration frames by median-combining individual calibration images and used them to correct the scientific images. A reference image was selected in each dataset and used to correct pointing variations. The target and a suitable set of non-variable comparison stars were identified in the images and three rings were placed interactively around them; the aperture radii were chosen based

² The acronym IDL stands for Interactive Data Language and is a trademark of ITT Visual Information Solutions.

on the lowest scatter achieved when compared with a fitted model. Differential photometry was finally measured using the APER routine³. Light curves were created with a second-order polynomial fitted to the out-of-transit data. The comparison star weights and polynomial coefficients were fitted simultaneously in order to minimise the scatter outside transit. Final light curves are plotted in Fig. 3 together with one, obtained by phasing/binning the four light curves reported in the discovery paper (Bakos et al. 2012), shown here just for comparison.

Very interestingly, the light curves present anomalies attributable to the passage of the planetary shadow over starspots or starspot complexes on the photosphere of the host star, which show up in weak and strong fashion. In particular, the transit observed with the Cassini telescope was also observed by the Toruń 0.6 m telescope (Maciejewski et al. 2013), which confirms the presence of anomalies in the light curves.

2.3. Photometric follow-up observations of WASP-11/HAT-P-10

A transit observation of WASP-11/HAT-P-10 b was performed on November 2009 with the Cassini 1.52 m telescope through a Gunn-*r* filter. Unfortunately, the weather conditions were not optimal and the data were badly affected by the poor transparency of the sky. The same transit monitored by HARPS-N (October 2, 2014) was also observed by the Zeiss 1.23 m telescope through a Cousins-*I* filter and a more adequate seeing ($\sim 0.7''$). The char-

³ APER is part of the ASTROLIB subroutine library distributed by NASA.

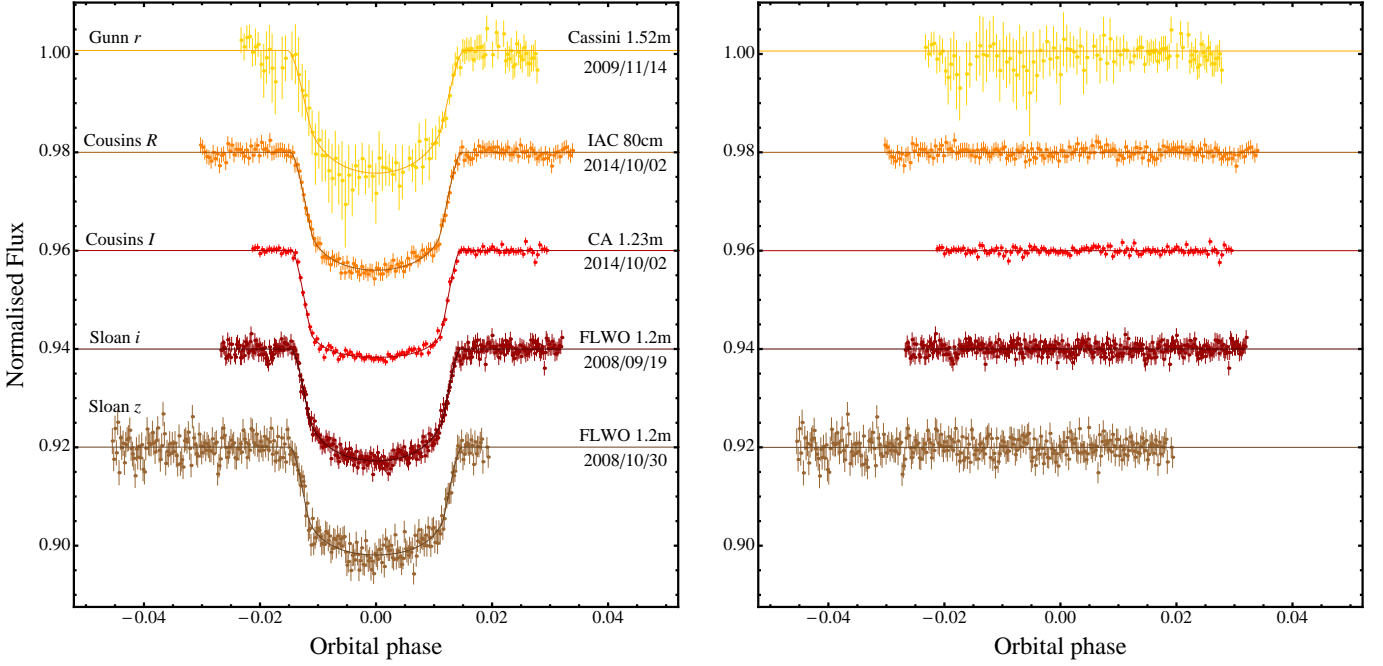


Fig. 4. Light curves of WASP-11/HAT-P-10b transits compared with the best JKTEBOP fits. The dates, the telescopes and the filters used for each transit event are indicated. Residuals from the fits are displayed in the *right panel*. Starting from the top, the first three light curves are from this work, whereas the last two are from Bakos et al. (2009). The second and third light curves are related to the same transit event.

Table 2. Details of the transit observations presented in this work.

Telescope	Date of first obs	Start time (UT)	End time (UT)	N_{obs}	T_{exp} (s)	T_{obs} (s)	Filter	Airmass	Moon illum.	Aperture radii (px)	Scatter (mmag)
HAT-P-36:											
Cassini	2013 04 14	19:58	00:39	112	120	144	Gunn <i>r</i>	1.05 → 1.000 → 1.17	12%	16,45,65	1.12
CA 1.23 m	2014 04 14	19:50	02:08	176	80-120	92-132	Cousins <i>I</i>	1.28 → 1.009 → 1.20	98%	22,50,75	1.10
CA 1.23 m	2014 04 18	19:54	00:26	146	80-130	92-142	Cousins <i>I</i>	1.22 → 1.009 → 1.06	92%	22,50,75	1.30
WASP-11/HAT-P-10:											
Cassini	2009 11 14	23:02	03:36	101	90-150	114-174	Gunn <i>r</i>	1.06 → 1.02 → 2.00	9%	17,25,45	2.24
CA 1.23 m	2014 10 02	00:51	05:23	125	120	132	Cousins <i>I</i>	1.12 → 1.04 → 1.21	52%	23,33,60	0.65
IAC 80 cm	2014 10 01	23:56	05:39	179	90	115	Cousins <i>R</i>	1.008 → 1.000 → 2.49	52%	28,60,90	0.92

Notes. N_{obs} is the number of observations, T_{exp} is the exposure time, T_{obs} is the observational cadence, and ‘Moon illum.’ is the geocentric fractional illumination of the Moon at midnight (UT). The aperture sizes are the radii of the software apertures for the star, inner sky and outer sky, respectively. Scatter is the *rms* scatter of the data versus a fitted model.

acteristics of the two telescopes and observation *modus operandi* were already described in the previous section. Moreover, the identical transit was observed with a third telescope, the IAC 80 cm telescope, located at the Teide Observatory on the island of Tenerife (Spain). The optical channel of this telescope is equipped with CAMELOT, a 2048×2048 CCD detector with a plate scale of $0.304 \text{ arcsec pixel}^{-1}$, providing an astronomical FOV of $10.4 \text{ arcmin} \times 10.4 \text{ arcmin}$. Details of these three WASP-11/HAT-P-10 b transit observations are reported in Table 2. The data sets were reduced in the same way as those for the HAT-P-36 case (Sect. 2.2) and the corresponding light curves are shown in Fig. 4, together with other two taken from Bakos et al. (2009). The simultaneous transit observation is highlighted in Fig. 5, and it allowed an extremely precise measurement of the mid-point transit time, i.e. $T_0 = 2\,456\,933.615069 \pm 0.000075 \text{ BJD(TDB)}$.

3. Light-curve analysis

The three HAT-P-36 light curves show possible starspot crossing events, which must be analysed using a self-consistent and physically realistic model. As in previous cases (Mancini et al. 2013b, 2014b; Mohler-Fischer et al. 2013), we utilise the PRISM⁴ and GEMC⁵ codes (Tregloan-Reed et al. 2013, 2015) to undertake this task. PRISM performs a modelling of planetary-transit light curves with one or more starspots by means of a pixellation approach in Cartesian coordinates. GEMC uses a Differential Evolution Markov Chain Monte Carlo (DE-MCMC) approach to locate the parameters of the PRISM model that better fit the data, using a global search. The fitted parameters of PRISM are the sum and ratio of the

⁴ Planetary Retrospective Integrated Star-spot Model.

⁵ Genetic Evolution Markov Chain.

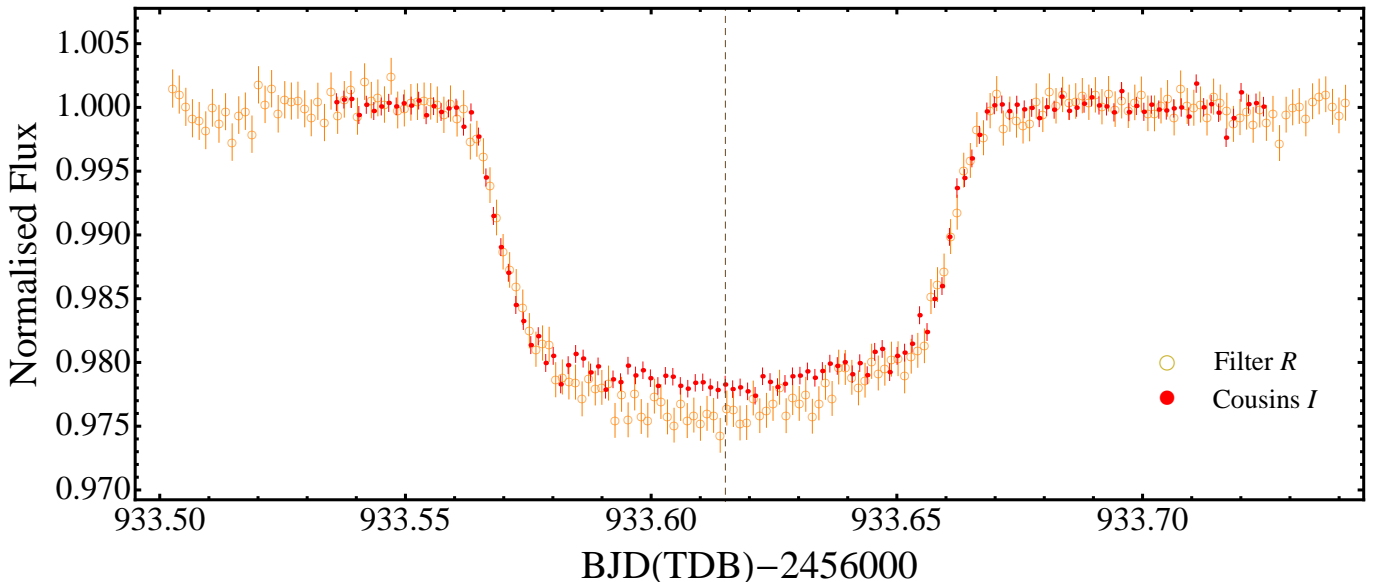


Fig. 5. Light curve of a transit event of WASP-11/HAT-P-10b observed simultaneously with the CA 1.23 m (red points) and the IAC 80 cm (empty orange circles) telescopes. The data of the two telescopes are superimposed to highlight the difference in the light-curve shape caused by the different filter adopted (Knutson et al. 2007). The dashed vertical line represents the time of transit mid-point that, thanks to the two-site strategy, was very accurately measured.

fractional radii⁶ ($r_A + r_b$ and $k = \frac{r_b}{r_A}$), the orbital period and inclination (P and i), the time of transit midpoint (T_0) and the coefficients of the quadratic limb darkening law (u_A and v_A).

The PRISM+GEMC code works in the way that the user has to decide how many starspots have to be fitted. We fitted for all the spot anomalies that can be seen in the transit light curves. Each starspot is then reproduced by the longitude and co-latitude of its centre (θ and ϕ), its angular radius (r_{spot}) and its contrast (ρ_{spot}), the last being the ratio of the surface brightness of the starspot to that of the surrounding photosphere. The orbital eccentricity was fixed to zero (Bakos et al. 2012).

The derived parameters of the planetary system are reported in Table 3, while those of the starspots in Table 4. The light curves and their best-fitting models are shown in Fig. 3. For each transit, a representation of the starspots on the stellar disc is drawn in Fig. 8.

The light curves for the WASP-11/HAT-P-10 transits were modelled by JKTEBOP⁷ (see Southworth 2008, 2013 and references therein), as this code is much faster than the previous one and no clear starspot anomalies are visible. The parameters used for JKTEBOP were the same as for PRISM and the orbital eccentricity was also fixed to zero (Bakos et al. 2009). Light curves from the second discovery paper (Bakos et al. 2009) were also reanalysed. The results of the fits are summarised in Table 5 and displayed in Fig. 4. Its low quality meant that the Cassini light curve (top curve in Fig. 4) was excluded from the analysis.

Table 6. Times of transit midpoint of HAT-P-36 b and their residuals.

Time of minimum BJD(TDB)–2400000	Cycle no.	O-C (JD)	Reference
55555.89060 ± 0.00043	-7	0.000376	1
55597.04088 ± 0.00770	24	0.002904	1
55601.01882 ± 0.00074	27	-0.001197	1
55608.98390 ± 0.00030	33	-0.000198	1
56365.56800 ± 0.00234	603	-0.001928	3
56397.42170 ± 0.00202	627	-0.004655	3
56397.42894 ± 0.00031	627	0.000822	2
56762.44834 ± 0.00018	902	-0.000158	3
56766.43055 ± 0.00028	905	-0.000011	3

Notes. References: (1) FLWO 1.2 m (Bakos et al. 2012); (2) Cassini 1.52 m (this work); (3) CA 1.23 m (this work).

3.1. Orbital period determination

We used the new photometric data to refine the transit ephemeris of HAT-P-36 b. The transit times and uncertainties were obtained using PRISM+GEMC as previously explained. To these timings, we added four from the discovery paper (Bakos et al. 2012) and two from Maciejewski et al. (2013)⁸. The nine timings were placed on the BJD(TDB) time system (Table 6). The resulting measurements of transit midpoints were fitted with a straight line to obtain a final orbital ephemeris

$$P = 1.32734684 \pm 0.00000050 \text{ d}$$

⁶ The fractional radii are defined as $r_A = \frac{R_*}{a}$ and $r_b = \frac{R_p}{a}$, where R_* and R_p are the true radii of the star and planet, and a is the orbital semimajor axis.

⁷ JKTEBOP is written in FORTRAN77 and is available at: <http://www.astro.keele.ac.uk/jkt/codes/jktebop.html>

⁸ We added 1/25 days to the published values to correct an error caused by a misunderstanding in reading the time stamps of the fits files.

Table 3. Photometric properties of the HAT-P-36 system derived by fitting the light curves with GEMC.

Source	Filter	$r_A + r_b$	k	i°	u_A	v_A
Cassini 1.52 m	Gunn r	0.2278 ± 0.0037	0.1243 ± 0.0025	85.95 ± 0.34	0.24 ± 0.13	0.40 ± 0.21
CA 1.23 m #1	Cousins I	0.2298 ± 0.0039	0.1290 ± 0.0023	85.76 ± 0.36	0.25 ± 0.10	0.29 ± 0.19
CA 1.23 m #2	Cousins I	0.2285 ± 0.0039	0.1298 ± 0.0012	85.86 ± 0.43	0.32 ± 0.11	0.15 ± 0.14

Table 4. Starspot parameters derived from the GEMC fitting of the HAT-P-36 transit light curves presented in this work.

Telescope	starspot	$\theta(^{\circ})^a$	$\phi(^{\circ})^b$	$r_{\text{spot}}(^{\circ})^c$	ρ_{spot}^d	Temperature (K) ^e
Cassini 1.52 m	#1	-36.59 ± 1.85	77.41 ± 5.82	11.42 ± 3.45	0.65 ± 0.07	5070 ± 129
	#2	38.29 ± 2.88	82.68 ± 5.27	12.54 ± 5.57	0.62 ± 0.23	5016 ± 421
CA 1.23 m #1	#1	21.06 ± 3.20	86.52 ± 3.96	17.67 ± 4.81	$0.86^{+0.14}_{-0.17}$	5380 ± 305
CA 1.23 m #2	#1	-24.99 ± 4.91	87.08 ± 3.17	21.38 ± 6.82	$0.92^{+0.08}_{-0.14}$	5485 ± 244
	#2	46.00 ± 14.13	88.27 ± 2.38	18.66 ± 3.52	0.78 ± 0.19	5253 ± 353

Notes. ^(a)The longitude of the centre of the spot is defined to be 0° at the centre of the stellar disc and can vary from -90° to 90° . ^(b)The co-latitude of the centre of the spot is defined to be 0° at the north pole and 180° at the south pole. ^(c)Angular radius of the starspot (note that an angular radius of 90° covers half of stellar surface). ^(d)Spot contrast; note that 1.0 equals the brightness of the surrounding photosphere. ^(e)The temperature of the starspots are obtained by considering the photosphere and the starspots as black bodies.

Table 5. Photometric properties of the WASP-11/HAT-P-10 system derived by fitting the light curves with JKTEBOP.

Source	Filter	$r_A + r_b$	k	i°	u_A	v_A
Cassini 1.52 m	Gunn r	0.10137 ± 0.01380	0.13639 ± 0.00868	88.00 ± 1.97	0.56 ± 0.23	0.21 ± 0.06
CA 1.23 m	Cousins I	0.09230 ± 0.00197	0.13234 ± 0.00078	89.09 ± 0.68	0.24 ± 0.04	0.25 ± 0.07
IAC 80 cm	Cousins R	0.09695 ± 0.00358	0.13657 ± 0.00200	88.29 ± 0.54	0.40 ± 0.08	0.21 ± 0.07
FLWO 1.2 m	Sloan z	0.09277 ± 0.00350	0.12818 ± 0.00181	89.95 ± 0.92	0.41 ± 0.06	0.27 ± 0.07
FLWO 1.2 m	Sloan i	0.09160 ± 0.00242	0.12856 ± 0.00156	89.94 ± 0.76	0.49 ± 0.05	0.25 ± 0.07

and the mid-transit time at cycle zero

$$T_0 = 2455565.18165 \pm 0.00037 \text{ BJD(TDB)},$$

with reduced $\chi^2_\nu = 2.5$, which is significantly greater than unity. A plot of the residuals around the fit (see Fig. 6) does not indicate any clear systematic deviation from the predicted transit times.

We introduced other 21 timings in the analysis measured based on transit light curves observed by amateur astronomers and available on the ETD⁹ website. These 21 light curves were selected considering if they had complete coverage of the transit and a Data Quality index ≤ 3 . Repeating the analysis with a larger sample, we obtained 4.1 as the reduced χ^2_ν of the fit. A high value of χ^2_ν means that the assumption of a constant orbital period does not agree with the timing measurements. This could indicate either transit timing variations (TTVs) or that the measurement errors are underestimated. The latter possibility can occur very easily, but be difficult to rule out, so the detection of TTVs requires more than just an excess χ^2_ν . The Lomb-Scargle periodogram generated for timing residuals shows no significant signal, making any periodic variation unlikely, so we do not claim the existence of TTVs in this system. The residuals of the ETD timings are also shown in Fig. 6 for completeness.

New mid-transit times (three transits; this work) and those available in the literature (9 transits) allowed us to

⁹ The Exoplanet Transit Database (ETD) website can be found at <http://var2.astro.cz/ETD>

Table 7. Times of transit midpoint of WASP-11/HAT-P-10 b and their residuals.

Time of minimum BJD(TDB)–2400000	Cycle no.	O-C (JD)	Reference
54729.90657 ± 0.00023	0	-0.000589	1
54770.85432 ± 0.00011	11	-0.000115	1
54793.19692 ± 0.00076	17	0.002071	2
55143.10895 ± 0.00046	111	0.001013	2
55161.71529 ± 0.00021	116	0.000490	3
55507.90419 ± 0.00042	209	-0.001219	3
55842.92921 ± 0.00021	299	0.000631	3
55842.92952 ± 0.00044	299	0.000941	3
55865.26734 ± 0.00166	305	-0.001483	2
55150.54662 ± 0.00104	113	-0.000741	4
56933.61504 ± 0.00008	592	-0.000086	5
56933.61522 ± 0.00018	592	0.000099	6

Notes. References: (1) FLWO 1.2 m (Bakos et al. 2009); (2) Wang et al. (2014); (3) Sada et al. (2012); (4) Cassini 1.52 m (this work); (5) CA 1.23 m (this work); (6) IAC 80 cm (this work).

refine transit ephemeris for WASP-11/HAT-P-10 b too. In particular, the two light curves from Bakos et al. (2009) were re-fitted with JKTEBOP (Fig. 4). All the timings are summarised in Table 7. As a result of a linear fit, in which timing uncertainties were taken as weights, we derived

$$P = 3.72247967 \pm 0.00000045 \text{ d}$$

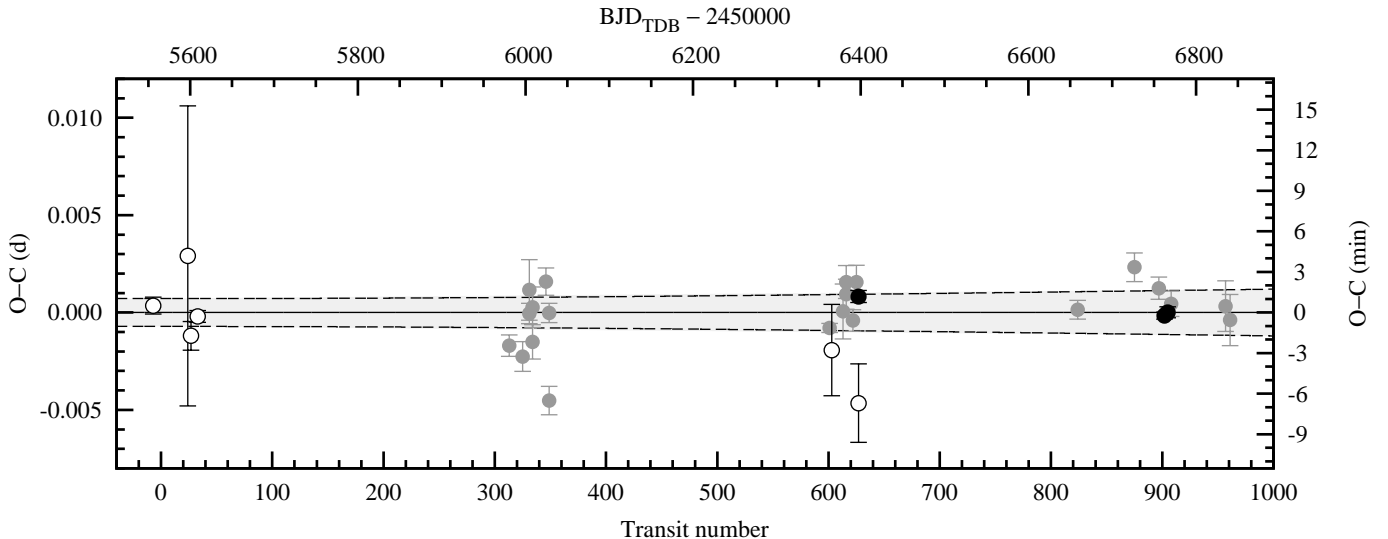


Fig. 6. Residuals for the timings of HAT-P-36 b at mid-transit versus a linear ephemeris. The four timings reported by Bakos et al. (2012) and the two by Maciejewski et al. (2013) are plotted using empty circles, while those marked with gray circles are from ETD. The timings measured by this work are shown with black circles. The dashed lines mark $2\text{-}\sigma$ uncertainties of the ephemeris (i.e. at the 95% confidence level), which was estimated without considering the data from ETD.

and the mid-transit time at cycle zero

$$T_0 = 2454729.90716 \pm 0.00020 \text{ BJD}_{\text{TDB}},$$

with $\chi^2_\nu = 5.0$, which is again far from unity. This could be explained again by underestimated timing uncertainties or hypothesizing a variation in transit times caused by unseen planetary companion or stellar activity. However, also for this case the Lomb-Scargle periodogram shows no significant signal, not supporting the second hypothesis. The plot of the residuals around the fit is shown in Fig. 7.

As in the previous case, we selected 34 transits from ETD, using the same criteria explained above. Most of the corresponding timings are very scattered around the predicted transit mid-times, but have tiny error bars. Including them in the fit returns a higher value for the χ^2_ν , suggesting that their uncertainties are very underestimated, and the data reported on ETD should be used cautiously. They are shown in Fig. 7.

We would like to stress however that, since in both the cases the timing measurements are in groups separated by several hundred of days, we are not sensitive to all the periodicities. Only by performing systematic observations of many subsequent transits it is possible to rule out the presence of additional bodies in the two TEP systems with higher confidence.

3.2. HAT-P-36 starspots

As described in Sect. 3, the anomalies in the three HAT-P-36 light curves were modelled as starspots, whose parameters were fitted together with those of the transits (see Tables 3 and 4). The stellar disc, the positions of starspots and the transit chords are displayed in Fig. 8, based on the results of the modelling. Considering both the photosphere and the starspots as black bodies (Rabus et al. 2009; Sanchis-Ojeda et al. 2011; Mohler-Fischer et al. 2013) and using Eq. 1 of Silva (2003) and $T_{\text{eff}} = 5620 \pm 40$ (see Sect. 4.1), we estimated the temperature of the starspots

at different bands and reported them in the last column of Table 4. The values of the starspot temperature estimated in the transit on April 2013 are in good agreement with each other within the experimental uncertainties. The same is true for those observed in the two transits on April 2014, even if they point to starspots with temperature higher than, but still compatible, with those of the previous year. The starspot temperatures measured from the Loiano and CAHA observations are consistent with what has been measured for other main-sequence stars in transit observations, as we can see from Fig. 9, where we report the starspot temperature contrast versus the temperature of the photosphere of the corresponding star for data taken from the literature. The spectral class of the stars is also reported and allows us to figure out that the temperature difference between photosphere and starspots is not strongly dependent on spectral type, as already noted by Strassmeier (2009).

The observations of multiple planetary transits across the same starspot or starspot complex could provide another type of precious information (Sanchis-Ojeda et al. 2011). Indeed, thanks to the good alignment between the stellar spin axis and the perpendicular to the planet's orbital plane, one can measure the shift in position of the starspot between the transit events and constrain the alignment between the orbital axis of the planet and the spin axis of the star with higher precision than from the measurement of the RM effect (e.g., Tregloan-Reed et al. 2013).

In our case, we have two consecutive transits observed in 2014 April 14 and 18 and we might wonder if the planet has crossed the same starspot complex in those transit events. According to Eq. 1 of Mancini et al. (2014b), the same starspot can be observed after consecutive transits or after some orbital cycles, presuming that in the latter case the star performs one or more rotations around its axis. Since the projected obliquity measured by the RM effect (see Sect. 4) indicates spin-orbit alignment, we expect to find similar values for the starspot parameters in our fits. Examining Table 4, we note that they seem to agree on co-

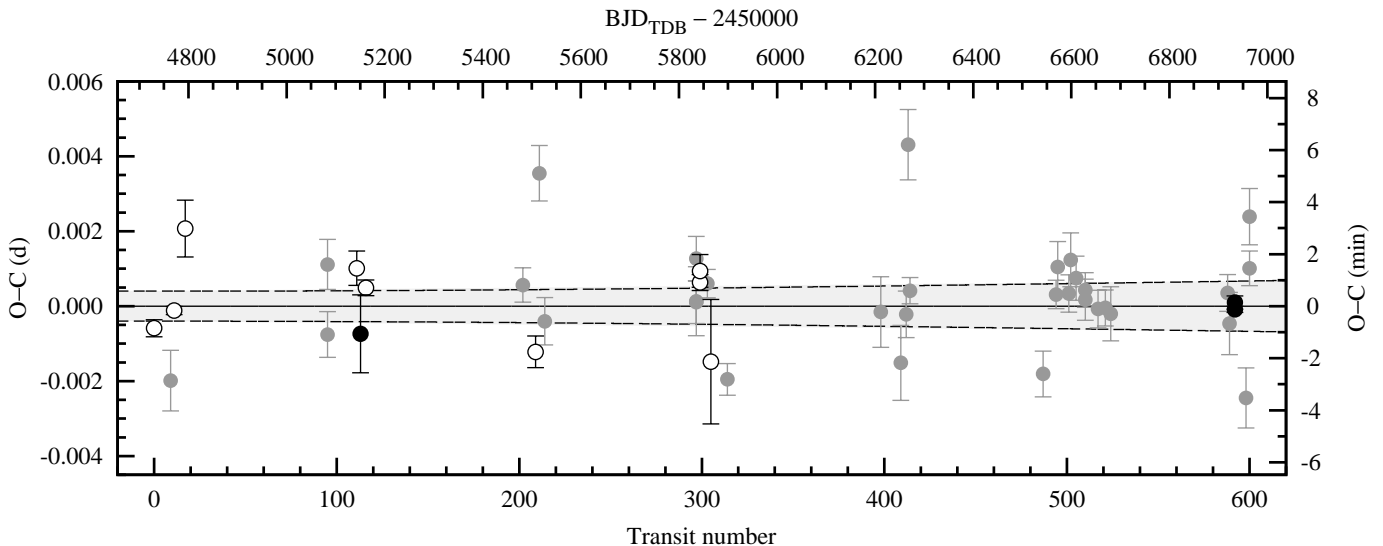


Fig. 7. Residuals for the timings of WASP-11/HAT-P-10 b at mid-transit versus a linear ephemeris. The filled black dots are from this work, open circles from the literature, (i.e. Bakos et al. 2009; Sada et al. 2012; Wang et al. 2014) and gray dots from ETD. The dashed lines mark $2\text{-}\sigma$ uncertainties of the ephemeris, which was estimated without considering the data from ETD.

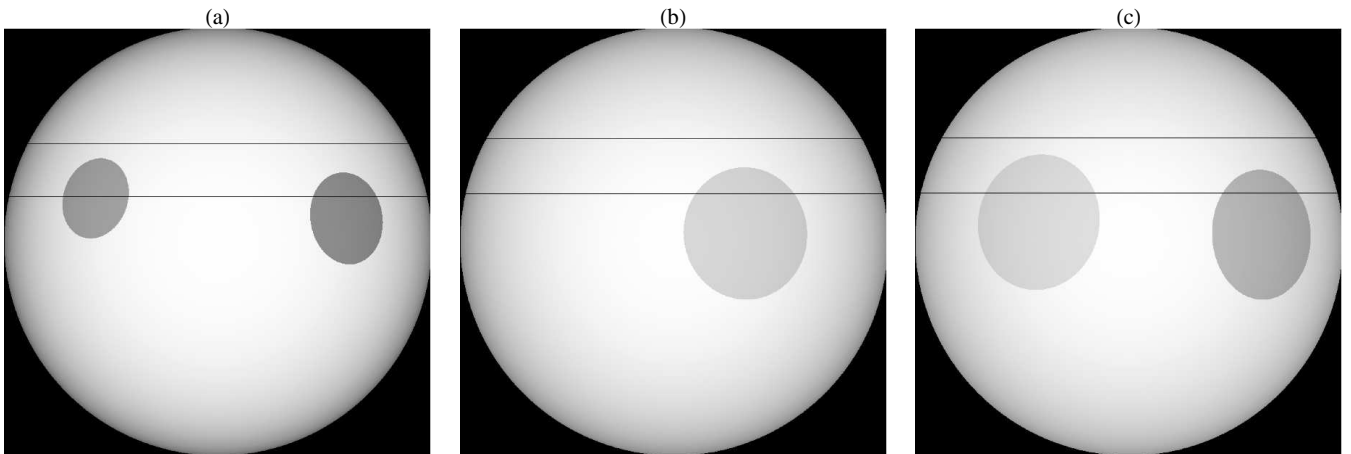


Fig. 8. Representation of the stellar disc, starspot positions and transit chord for the three HAT-P-36 datasets containing spot anomalies: (a) refers to the transit observed with the Cassini 1.52 m telescope on 2013 April 15, while (b) and (c) to those observed with the CA 1.23 m telescope on 2014 April 14 and 18, respectively. The gray scale of each starspot is related to its contrast (compare with values in Table 4).

latitude, size and contrast within their $1\text{-}\sigma$ errors. Owing to its size, the starspot on April 14 should still be seen four days later (if it is on the visible side of the star). That means that the starspot should have travelled $\sim 315^\circ$ in four days, giving a rotation period of ~ 4.57 days, which is too fast compared with that at the stellar equator estimated from the sky-projected rotation rate and the stellar radius, that is

$$P_{\text{rot}} \approx \frac{2\pi R_\star}{v \sin i_\star} \sin i_\star = (16.9 \pm 4.3 \text{ d}) \sin i_\star, \quad (1)$$

where i_\star is the inclination of the stellar rotation axis with respect to the line of sight. If we consider reversing the rotational direction so that the starspot is travelling right to left, then the starspot had to travel for $\sim 45^\circ$ in four days; but this implies that the stellar rotation period at co-latitude of 87° would be now too large (~ 32 days) and that HAT-P-36 b has a retrograde orbit. Since the latter

hypothesis is excluded by the geometry of the RM effect that we observed (see Sect. 4.3) and since four days are not sufficient for the starspot to rotate around the back of the star and then appear on the left hemisphere, we conclude that the starspot observed on 2014 April 14 is different from those on April 18.

3.3. Frequency analysis of the time-series light curves

In addition to the new photometric measurements of the transits presented in this work, dense time-series light curves are available in the WASP and HAT archives/databases for both the stars. These data are potentially very useful for detecting the signatures of the rotational period of each of the two stars. This is particularly true for the case of HAT-P-36, since the starspots detected in the photometric light curves (see previous section) indicate that this star is active. A further confirmation of this

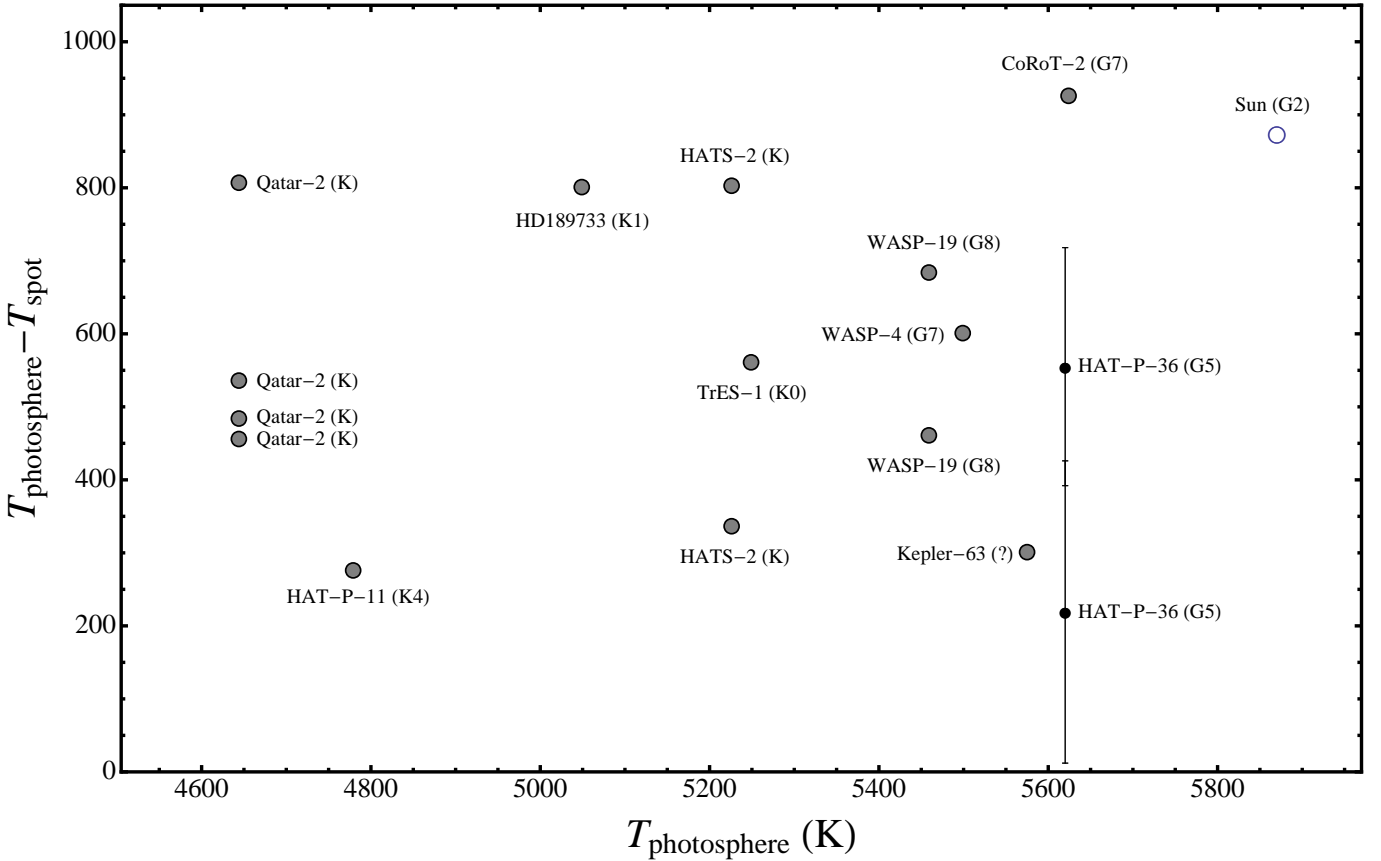


Fig. 9. Starspot temperature contrast with respect to the photospheric temperature in several dwarf stars. The name and spectral type of the star are also reported. The values for TrES-1, CoRoT-2, HD 189733, WASP-4, HATS-2, Kepler-63, Qatar-2 are taken from Rabus et al. (2009), Silva-Valio et al. (2010), Sing et al. (2011), Sanchis-Ojeda et al. (2011), Mohler-Fischer et al. (2013), Sanchis-Ojeda et al. (2013), Mancini et al. (2014b), respectively. The two values for WASP-19 are from Mancini et al. (2013b) and Huitson et al. (2013). The value of the Sun was taken from Berdyugina (2005). The error bars have been suppressed for clarity. Note that some stars appear twice or more. The black dots refer to the values estimated for the case of HAT-P-36 (this work). In particular, the lower is the value estimated by taking the weighted mean from the starspots detected with the Cassini telescope in April 2013, while the higher value was calculated from starspots detected with the CA 1.23 m telescope in April 2014.

activity is also given by the spectral analysis, as seen in Sect. 4.2.

We retrieved the photometric time series for HAT-P-36 (SDSS *r* filter) and WASP-11/HAT-P-10 (*I* Bessel filter) from the HAT public archive¹⁰; more specifically, we used the magnitudes data sets tagged as TF1 (Kovács et al. 2005). The WASP data available for WASP-11/HAT-P-10 were downloaded from the NASA Exoplanet Archive¹¹. The in-transit data points were removed from the light curve of each dataset.

The frequency analysis of the WASP and HAT time-series data related to WASP-11/HAT-P-10 did not detect any significant periodicity. Only the HAT data show a non-significant peak at $f = 0.034 \text{ d}^{-1}$. It is close to the synodic month, and the folded light curve shows a gap in the phase coverage corresponding to the Full Moon epochs. Therefore, it has been recognized as a spurious peak due to a combination of instrumental effects and spectral window.

On the other hand, the analysis of the HAT time-series light curve of HAT-P-36 (see Fig. 10) provided more inter-

esting results. After removing the transit data, the time-series light curve is composed of 9891 measurements. Both the iterative sine-wave fitting method (ISWF; Vaniček 1971) and the Lomb-Scargle periodogram supplied a lower peak at $f = 0.066 \text{ d}^{-1}$ and a higher one at $2f = 0.13 \text{ d}^{-1}$. Figure 11 shows the power spectrum obtained with the ISWF method. The amplitudes of the $2f$ and f components are 1.40 ± 0.15 and 0.88 ± 0.15 mmag, respectively. Since the level of the noise is 0.2 mmag, both are greater than the $S/N = 4.0$ significance threshold (Kuschnig et al. 1997). Moreover, the harmonics $3f$ and $4f$ are both clearly visible, the latter being more relevant than the former. HAT-P-36 was measured several times per night and often over night. Hence we could calculate 97 night averages (red points in Fig. 10). The frequency analysis of these averages supplied the same results as the single measurements.

When the even harmonics have amplitudes larger than those of the odd ones, the resulting light curve is shaped as a double wave. Since we know that the star is seen equator-on (see Sect. 4.3), such a light curve can easily be due to two groups of starspots that are alternatively visible to the observer. This is an independent confirmation of the spot model suggested in the previous subsection. We determined

¹⁰ <http://hatnet.org>

¹¹ <http://exoplanetarchive.ipac.caltech.edu/>

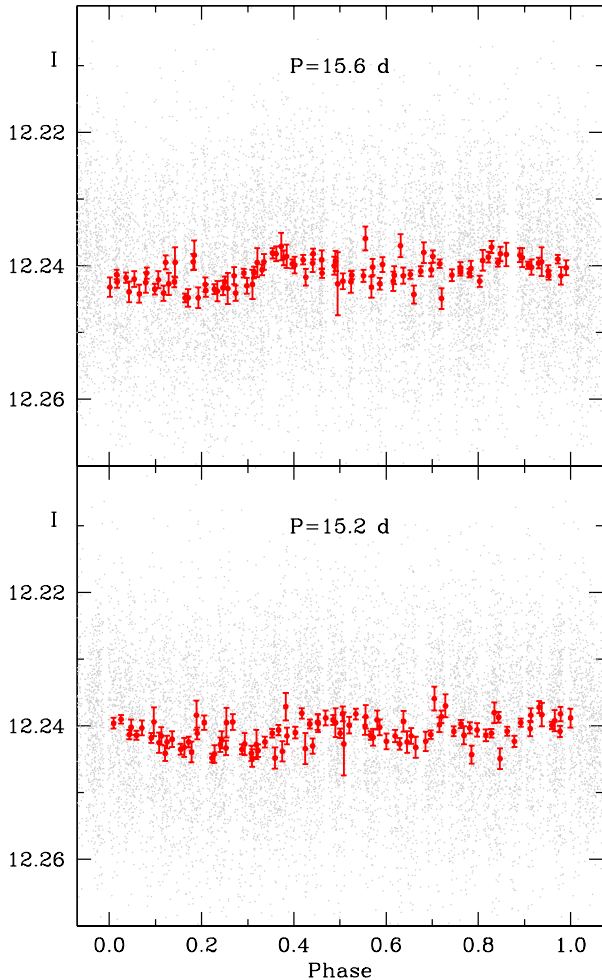


Fig. 10. *Top panel:* Single measurements (grey dots) and average values on single nights (red circles with errorbars) folded with $P = 15.6$ d, the best period obtained fitting the data with f and $2f$ fixed. *Bottom panel:* Single measurements (grey dots) and average values (red circles with errorbars) folded with $P = 15.2$ d, the best period obtained leaving the frequencies free to vary.

the rotational period in two ways. First, we searched for the best fit by fixing the frequency f and its harmonic $2f$. This procedure yields $P_{\text{rot}} = 15.2 \pm 0.3$ d. Then, we supposed that the differential rotation and the spread in longitude did not justify this condition, so we left the two frequency values free to vary, obtaining $P_{\text{rot}} = 15.6 \pm 0.1$ d. The periods are the same within the error bars and in excellent agreement with the period inferred from the stellar parameters, see Eq. (1). We merged the two determinations into $P_{\text{rot}} = 15.3 \pm 0.4$ d to cover both values and respective errorbars. The HAT-P-36 light curve is shown in Fig. 10, phase-folded with $P_{\text{rot}} = 15.6$ (top panel) and $P_{\text{rot}} = 15.2$ (bottom panel) days.

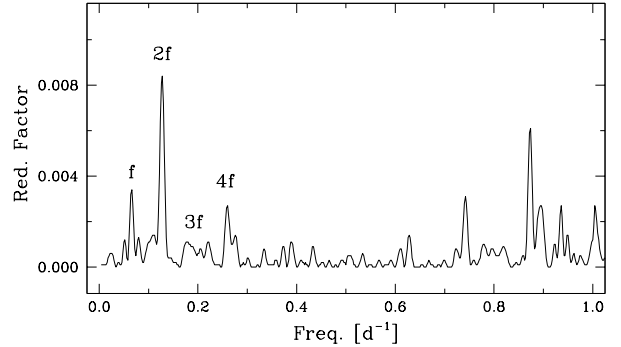


Fig. 11. Power spectrum of the original data of HAT-P-36, after removing the measurements during transit events.

4. HARPS-N spectra analysis

4.1. Spectroscopic determination of stellar atmospheric parameters

The effective temperature (T_{eff}), surface gravity ($\log g_{\star}$), iron abundance ($[\text{Fe}/\text{H}]$) and microturbulence velocity (v_{mic}) of the two host stars were derived by using the spectral analysis package MOOG (Snedden 1973, version 2013), and the equivalent widths (EWs) of iron lines, as described in detail in Biazzo et al. (2012). The EWs were measured on the mean spectrum obtained by averaging all the HARPS-N spectra available for each of the two stars. Here, T_{eff} was determined by imposing the condition that the Fe I abundance does not depend on the excitation potential of the lines, the microturbulence velocity, by requiring that the Fe I abundance is independent on the line EWs, and $\log g_{\star}$ by the Fe I/Fe II ionization equilibrium condition. The results are reported in Tables 8 and 9, for HAT-P-36 and WASP-11, respectively. The projected rotational velocity was estimated by means of spectral synthesis analysis with MOOG, yielding $v \sin i_{\star}$ values of 3.0 ± 0.5 km s $^{-1}$ and 0.9 ± 0.5 km s $^{-1}$ for HAT-P-36 and WASP-11, respectively, which are consistent, within the errors, with those obtained from the RM effect modelling (see Sect. 4.3).

4.2. Stellar activity index

The median values of the stellar activity index estimated from the HARPS-N spectra turned out to be $\log R'_{\text{HK}} = -4.636 \pm 0.066$ dex for HAT-P-36 and -4.848 ± 0.029 dex for WASP-11/HAT-P-10, indicating a moderate and low activity, respectively (e.g. Noyes et al. 1984). These values agree with what we have found in Sect. 3.3 by analysing the big photometric data sets from the HATNet and WASP surveys. The above values were obtained by adopting $B-V = 0.719$ and 0.989 , respectively, based on the stellar effective temperature and the color- T_{eff} conversion table by Casagrande et al. (2010). Knutson et al. (2010) found $\log R'_{\text{HK}} = -4.823$ dex for WASP-11/HAT-P-10 (estimated considering $B-V = 1.01$), which is in good agreement with our value.

Thanks to the activity index, we can also assess the expected rotation period from the level of the stellar activity, obtaining for HAT-P-36 $P_{\text{rot}} = 18.3 \pm 3.1$ d and 18.7 ± 2.9 d using Noyes et al. (1984) and Mamajek & Hillenbrand (2008) calibration scales, respectively, in quite good agreement, within the observational uncertainties, with what

was estimated in Sect. 3.3. For WASP-11/HAT-P-10, we obtained 40.8 ± 1.8 d and 40.9 ± 2.2 d, respectively.

Finally, we can get a clue on stellar age by applying the activity-age calibration proposed by Mamajek & Hillenbrand (2008), obtaining 2 Gyr and 5 Gyr for HAT-P-36 and WASP-11/HAT-P-10, respectively. However, we notice that the ages derived from stellar rotation and activity could be altered in the TEP systems because of star-planet tidal interactions, and any discrepancy with the values derived from the isochrones (see Sect. 5) may be due to this.

4.3. Determination of the spin-orbit alignment

The analysis of the photometric data allowed us a direct measurement, without reliance on theoretical stellar models, of the stellar mean density, ρ_* (Seager & Mallén-Ornelas 2003; Sozzetti et al. 2007) and, in combination with the spectroscopic orbital solution, the planetary surface gravity, g_p (Southworth et al. 2007), for each system. Exploiting the measured values of ρ_* , T_{eff} and $[\text{Fe}/\text{H}]$, we made use of the Yonsei-Yale evolutionary tracks (Demarque et al. 2004) to determine stellar characteristics, including M_* and R_* . The HARPS-N RV data sets were then fitted using a model that accounts both for the RV orbital trend and the RM anomaly.

We used the RM model that was elaborated and described in Covino et al. (2013) and Esposito et al. (2014), and we used the same least-square minimization algorithm to adjust it to the data. We set as free the barycentric radial velocity, γ , the mass of the planet, M_p , the projected stellar rotational velocity, $v \sin i_*$, the projected spin-orbit angle, λ and the linear limb-darkening coefficient u . All the other relevant parameters were kept fixed to the values determined from the spectroscopic and light curves analysis. The best-fitting RV models are illustrated in Fig. 1 and 2, superimposed on the datasets. In particular, the sky-projected spin-orbit misalignment angle was $\lambda = -14 \pm 18$ deg for HAT-P-36 and $\lambda = 7 \pm 5$ deg for WASP-11/HAT-P-10, indicating an alignment of the stellar spin with the orbit of the planet for both the systems. The final error bars were computed by a bootstrapping approach. The greater uncertainty in HAT-P-36 is of course because the transit was not completely observed. The reduced χ^2_ν maps in the $\lambda - v \sin i_*$ plane do not point out any clear correlation between λ and $v \sin i_*$.

The precise knowledge of the rotational period of a star, allows estimating the stellar spin inclination angle, i_* , and thus the true spin-orbit alignment angle, ψ . This is exactly the case for HAT-P-36, for which the analysis of the long time-series data set recorded by HATNet survey allowed us to determine the stellar rotational period. By using $P_{\text{rot}} = 15.3 \pm 0.4$ d (Sect. 3.3), we estimated that $i_* = 65^\circ \pm 34^\circ$. Then, we used Eq. (7) in Winn et al. (2007),

$$\cos \psi = \cos i_* \cos i + \sin i_* \sin i \cos \lambda, \quad (2)$$

to derive the true misalignment angle, obtaining $\psi = 25^{+36}_{-25}$. The major source of error in the determination of both i_* and ψ , estimated through the propagation of uncertainties, comes from the large relative error in the measurement of $v \sin i_*$; the observation of a full transit would have reduced the errors by a factor of 2 or more.

5. Physical parameters of the two systems

For calculating the full physical properties of each planetary system, we used the HSTEP methodology (see Southworth 2012, and references therein). The values of the photometric parameters $r_A + r_b$, k and i were first combined into weighted means. The orbital eccentricity was fixed to zero. We added in the measured P from the light curve analysis, T_{eff} and $[\text{Fe}/\text{H}]$ from the spectroscopic analysis, and the velocity semi-amplitude of the star, K_A , measured from the RVs. For K_A we used the values from Bakos et al. (2012) and Bakos et al. (2009). These come from spectra with reasonable coverage of the orbits of the host stars, so are more precise than our own values which come from data obtained only during or close to transit. We estimated a starting value for the velocity semi-amplitude of the planet, K_p , and used this to determine a provisional set of physical properties of the system using standard formulae (e.g., Hilditch 2001).

We then interpolated within a set of tabulated predictions from a theoretical stellar model to find the expected stellar radius and T_{eff} for our provisional mass and the observed $[\text{Fe}/\text{H}]$. The value of K_p was then iteratively refined to maximise the agreement between the observed and predicted T_{eff} , and the provisional $(R_A + R_b)/a$ and measured $r_A + r_b$ values. This K_b was then used alongside the other quantities given above to determine the physical properties of the system. This process was performed over all possible ages for the stars, from the zero-age to the terminal-age main sequence, and the overall best-fitting age and resulting physical parameters found.

The above process was performed using each of five different sets of theoretical models: Claret (Claret 2004), Y² (Demarque et al. 2004), BaSTI (Pietrinferni et al. 2004), VRSS (VandenBerg et al. 2006) and DSEP (Dotter et al. 2008). The final result of this analysis was five sets of properties for each system, one from each of the five sources of theoretical models (see Tables A.1 and A.2). For the final value of each output parameter, we calculated the unweighted mean of the five estimates from using the different sets of model predictions. Statistical errorbars were propagated from the errorbars in the values of all input parameters. Systematic errorbars were assigned based on the inter-agreement between the results from the five different stellar models.

Tables 8 and 9 give the physical properties we found for HAT-P-36 and WASP-11, respectively. Our results are in good agreement, but they are more precise than previous determinations.

6. Discussion

As introduced in Sect. 1, orbital obliquity could be an important parameter to determine in order to trace the physical processes that happened during migration phase of current hot Jupiters. Several empirical trends have been presented to corroborate this hypothesis. TEP systems, in which the parent star is relatively cool ($T_{\text{eff}} \lesssim 6100$ K), should be much more aligned than those with hotter stars, because the realignment of cool star's convective envelopes can occur on timescales shorter than planet's orbital decay (Winn et al. 2010; Albrecht et al. 2012b; Dawson 2014). The larger spin-orbit misalignment expected for the hot stars (F-type stars with $T_{\text{eff}} > 6100 - 6200$ K) could be

Table 8. Physical parameters of the planetary system HAT-P-36 derived in this work.

Parameter	Nomen.	Unit	This Work	Bakos et al. (2012)
Stellar parameters				
Spectral class			G5 V	...
Effective temperature	T_{eff}	K	5620 ± 40	5560 ± 100
Metal abundance	[Fe/H]		$+0.25 \pm 0.09$	$+0.26 \pm 0.10$
Projected rotational velocity	$v \sin i_*$	km s^{-1}	3.12 ± 0.75	3.58 ± 0.5
Rotational period	P_{rot}	days	15.3 ± 0.4	...
Linear LD coefficient	u		0.81 ± 0.17	...
Mass	M_*	M_{\odot}	$1.030 \pm 0.029 \pm 0.030$	1.022 ± 0.049
Radius	R_*	R_{\odot}	$1.041 \pm 0.013 \pm 0.010$	1.096 ± 0.056
Mean density	ρ_*	ρ_{\odot}	0.913 ± 0.027	...
Logarithmic surface gravity	$\log g_*$	cgs	$4.416 \pm 0.010 \pm 0.004$	4.37 ± 0.04
Age		Gyr	$4.5^{+2.4+3.1}_{-1.4-2.8}$	$6.6^{+2.9}_{-1.8}$
Planetary parameters				
Mass	M_{p}	M_{Jup}	$1.852 \pm 0.088 \pm 0.036$	1.832 ± 0.099
Radius	R_{p}	R_{Jup}	$1.304 \pm 0.021 \pm 0.013$	1.264 ± 0.071
Mean density	ρ_{p}	ρ_{Jup}	$0.737 \pm 0.095 \pm 0.007$	0.84 ± 0.14
Surface gravity	g_{p}	m s^{-2}	27.0 ± 1.4	28 ± 3
Equilibrium temperature	T_{eq}	K	1788 ± 15	1823 ± 55
Safronov number	Θ		$0.0658 \pm 0.0030 \pm 0.0006$	0.067 ± 0.005
Orbital parameters				
Time of mid-transit	T_0	BJD(TDB)	$2\,455\,565.18167 \pm 0.00036$	$2\,455\,565.18144 \pm 0.00020$
Period	P_{orb}	days	1.32734683 ± 0.0000048	1.327347 ± 0.000003
Semi-major axis	a	au	$0.02388 \pm 0.00022 \pm 0.00023$	0.0238 ± 0.0004
Inclination	i	degree	85.86 ± 0.21	86.0 ± 1.3
RV-curve semi-amplitude	K_{A}	m s^{-1}	316 ± 39^a	334.7 ± 14.5
Barycentric RV	γ	km s^{-1}	-16.327 ± 0.006	-16.29 ± 0.10
Projected spin-orbit angle	λ	degree	-14 ± 18	...
True spin-orbit angle	ψ	degree	25^{+38}_{-25}	...

Notes. Where two errorbars are given, the first refers to the statistical uncertainties and the second to the systematic errors.

^a This value of K_{A} was determined from our RV data, which were taken during transit time only. The value reported by Bakos et al. (2009), which is based on RV data with a much better coverage of the orbital phase, was therefore preferred for the determination of the other physical parameters of the system (see Sect.5).

also explained by considering they have a smaller convective zone than that of the cool stars. This implies that the tidal dissipation is much less efficient for the hot stars than the cold ones (Lai 2012; Valsecchi & Rasio 2014).

It was also noted that TEP systems in which the hot Jupiter is massive ($M_{\text{p}} \gtrsim 3 M_{\text{Jup}}$) tend to have lower spin-orbit angles, the parent star being much more affected by planet's tidal influence (Hébrard et al. 2011). However, several theoretical studies were not able to explain the above correlations (e.g., Rogers & Lin 2013; Xue et al. 2014) and, as stressed by Esposito et al. (2014), there are planetary systems composed by cool stars that are highly misaligned.

With this work, we contribute to enlarge the sample, adding the measurement of the sky-projected orbital obliquity for other two TEP systems. They are HAT-P-36 and WASP-11/HAT-P10, both composed by stars with $T_{\text{eff}} < 6100 \text{ K}$, whose spin results to be well aligned with the planetary-orbit axis. They are reported in Fig. 12 (black circles), together with the other 82 known TEP systems¹², as a function of stellar effective temperature, projected rotational velocity, eccentricity, orbital period, planetary mass and stellar metallicity. Following Dawson (2014), we divided the data in two groups, based on the parent stars temperature; they are shown with orange circles if $T_{\text{eff}} > 6100 \text{ K}$ and with empty circles for the opposite case. An inspection of these plots does not allow to highlight any clear

trend, but, on the contrary, the values of λ are quite randomly distributed in the various parameter spaces, suggesting that the observed diversity of stellar obliquities may be a consequence of more complicated interactions with outer planets.

We also plotted in Fig. 13 the projected orbital obliquity of the cool-star systems, i.e., following Anderson et al. (2015), those with $T_{\text{eff}} < 6150 \text{ K}$, as a function of orbital distance in units of stellar radii, a/R_* . However, we do not see an absolute confinement of λ at any particular orbital-separation range.

According to TEPcat, there are now 12 TEP systems for which we have the measurement of the true obliquity, i.e. the angle, ψ , between the axes of the stellar rotation and the planetary orbit. These values are plotted against the stellar temperature in Fig. 14 that, again, does not highlight any correspondence between the two quantities.

Based on a recent gyrochronology work by Meibom et al. (2015), the rotation period of HAT-P-36, estimated in Sect. 3.3, should correspond to an age of about 1.8 Gyr, which is close to the lower limit reported in Table 8, as derived from our isochrone-fitting analysis. Since the planet is very close to its host, we may speculate about tidal interactions affecting the evolution of the orbit and of the stellar spin. Assuming a modified tidal quality factor $Q'_* = 10^6$, the remaining lifetime of the system – i.e., the time left before the planet plunges into the star – is only 35 Myr (Metzger et al. 2012). Such a rapid orbital decay should be accompanied by a negative transit

¹² The data were taken from TEPcat (Southworth 2011). The brown dwarfs KELT-1 and WASP-30 were excluded from the sample.

Table 9. Physical parameters of the planetary system WASP-11/HAT-P-10 derived in this work.

Parameter	Nomen. / Unit	This Work	West et al. (2009)	Bakos et al. (2009)	Wang et al. (2014)
Stellar parameters					
Spectral Class		K3 V	K	K	...
Effective temperature	T_{eff} (K)	4900 ± 65	4800 ± 100	4980 ± 60	...
Metal abundance	[Fe/H]	$+0.12 \pm 0.09$	$+0.0 \pm 0.2$	$+0.13 \pm 0.08$...
Proj. rotational velocity	$v \sin i_*$ (km s $^{-1}$)	1.04 ± 0.15	< 6.0	0.5 ± 0.2	...
Linear LD coefficient	u	0.78 ± 0.16
Mass	M_* (M_{\odot})	$0.806 \pm 0.038 \pm 0.013$	$0.77_{-0.08}^{+0.10}$	0.83 ± 0.03	0.862 ± 0.014
Radius	R_* (R_{\odot})	$0.772 \pm 0.014 \pm 0.004$	$0.74_{-0.03}^{+0.04}$	0.79 ± 0.02	$0.784_{-0.011}^{+0.018}$
Mean density	ρ_* (ρ_{\odot})	1.748 ± 0.074	$1.789_{-0.116}^{+0.072}$
Logarithmic surface gravity	$\log g_*$ (cgs)	$4.569 \pm 0.018 \pm 0.002$	4.45 ± 0.20	4.56 ± 0.02	...
Age	(Gyr)	$7.6_{-3.0-1.8}^{+5.8+1.6}$...	7.9 ± 3.8	...
Planetary parameters					
Mass	M_p (M_{Jup})	$0.492 \pm 0.023 \pm 0.005$	0.53 ± 0.07	0.487 ± 0.018	0.526 ± 0.019
Radius	R_p (R_{Jup})	$0.990 \pm 0.022 \pm 0.005$	$0.91_{-0.03}^{+0.06}$	$1.005_{-0.027}^{+0.032}$	$0.999_{-0.018}^{+0.029}$
Mean density	ρ_p (ρ_{Jup})	$0.475 \pm 0.026 \pm 0.002$	$0.69_{-0.11}^{+0.07}$	0.594 ± 0.052	$0.526_{-0.046}^{+0.035}$
Surface gravity	g_p (m s $^{-2}$)	12.45 ± 0.50	$14.45_{-1.33}^{+1.66}$	12.02 ± 0.83	...
Equilibrium temperature	T_{eq} (K)	992 ± 14	960 ± 70	1020 ± 17	$1006.5_{-14.6}^{+16.4}$
Safronov number	Θ	$0.0539 \pm 0.0019 \pm 0.0003$...	0.053 ± 0.002	...
Orbital parameters					
Time of mid-transit	T_0 (BJD $_{\text{TDB}}$)	$2\,454\,729.90716 \pm 0.00020$	$2\,454\,473.05588 \pm 0.00020$	$2\,454\,759.68683 \pm 0.00016$	$2\,454\,808.07904 \pm 0.00012$
Period	P_{orb} (days)	$3.72247967 \pm 0.00000045$	3.722465 ± 0.000007	3.7224747 ± 0.0000065	$3.72247669 \pm 0.00000181$
Semi-major axis	a (au)	$0.04375 \pm 0.00070 \pm 0.00023$	0.043 ± 0.002	0.0435 ± 0.0006	0.04473 ± 0.00024
Inclination	i (degree)	89.03 ± 0.34	$89.8_{-0.8}^{+0.2}$	$88.6_{-0.4}^{+0.5}$	$89.138_{-0.470}^{+0.503}$
RV curve semi-amplitude	K_A (m s $^{-1}$)	82.7 ± 4.2^a	82.1 ± 7.4	74.5 ± 1.8	$76.16_{-2.58}^{+2.67}$
Barycentric RV	γ (km s $^{-1}$)	4.8951 ± 0.0021	4.9077 ± 0.0015	3.95 ± 0.43	...
Proj. spin-orbit angle	λ (degree)	7 ± 5

Notes. Where two errorbars are given, the first refers to the statistical uncertainties and the second to the systematic errors.

^a This value of K_A was determined from our RV data, which were taken during transit time only. The value reported by Bakos et al. (2009), which is based on RV data with a much better coverage of the orbital phase, was therefore preferred for the determination of the other physical parameters of the system (see Sect.5).

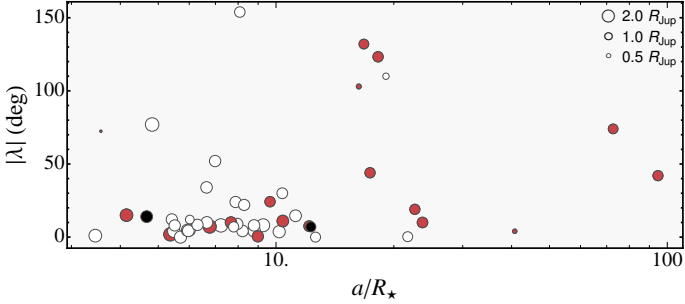


Fig. 13. The projected orbital obliquity as a function of scaled orbital distance, a/R_* , for those systems with $T_{\text{eff}} < 6150$ K (Anderson et al. 2015). The empty circles represent near-circular orbits ($e < 0.1$ or consistent with zero), while the light-red circles depict eccentric orbits. The size of each circle is proportional to the corresponding planetary radius. The data have been taken from TEPcat (Southworth 2011). The black points indicate the two TEP systems examined in this work, HAT-P-36 and WASP-11/HAT-P-10. The error bars have been suppressed for clarity.

time variation O-C of about 20 seconds in ten years that would be easy to measure with a space-borne photometer. On the other hand, if we assume $Q'_* \sim 10^7 - 10^8$, as suggested by Ogilvie & Lin (2007), the orbital decay and

alignment timescales are of the order of a few hundred Myr or a few Gyr, respectively. They are shorter than or comparable to the estimated age of the star. In conclusion, in this scenario the present alignment could result from the tidal interaction during the main-sequence lifetime, while the remaining lifetime of the system is at least of a few hundred Myr. In any case, HAT-P-36 is an interesting system to study the orbital and stellar spin evolution, as resulting from the tidal interaction and the magnetic wind braking of the star.

For WASP-11, the relatively large semi-major axis and the small mass of the planet imply, on the other hand, a weak tidal interaction with an angular momentum exchange timescale that is comparable or longer than the age of the star. Therefore, the observed projected alignment of the system is likely to be of primordial origin.

7. Summary and conclusions

In the framework of the GAPS programme, we are observing a sample of TEP systems hosting close-in hot Jupiters, with the HARPS-N spectrograph. The goal is to measure their spin-orbit alignment (by observing the RM effect) and study if this quantity is correlated with other physical properties. Here, we have presented an exhaustive study of the HAT-P-36 and WASP-11/HAT-P10 planetary systems,

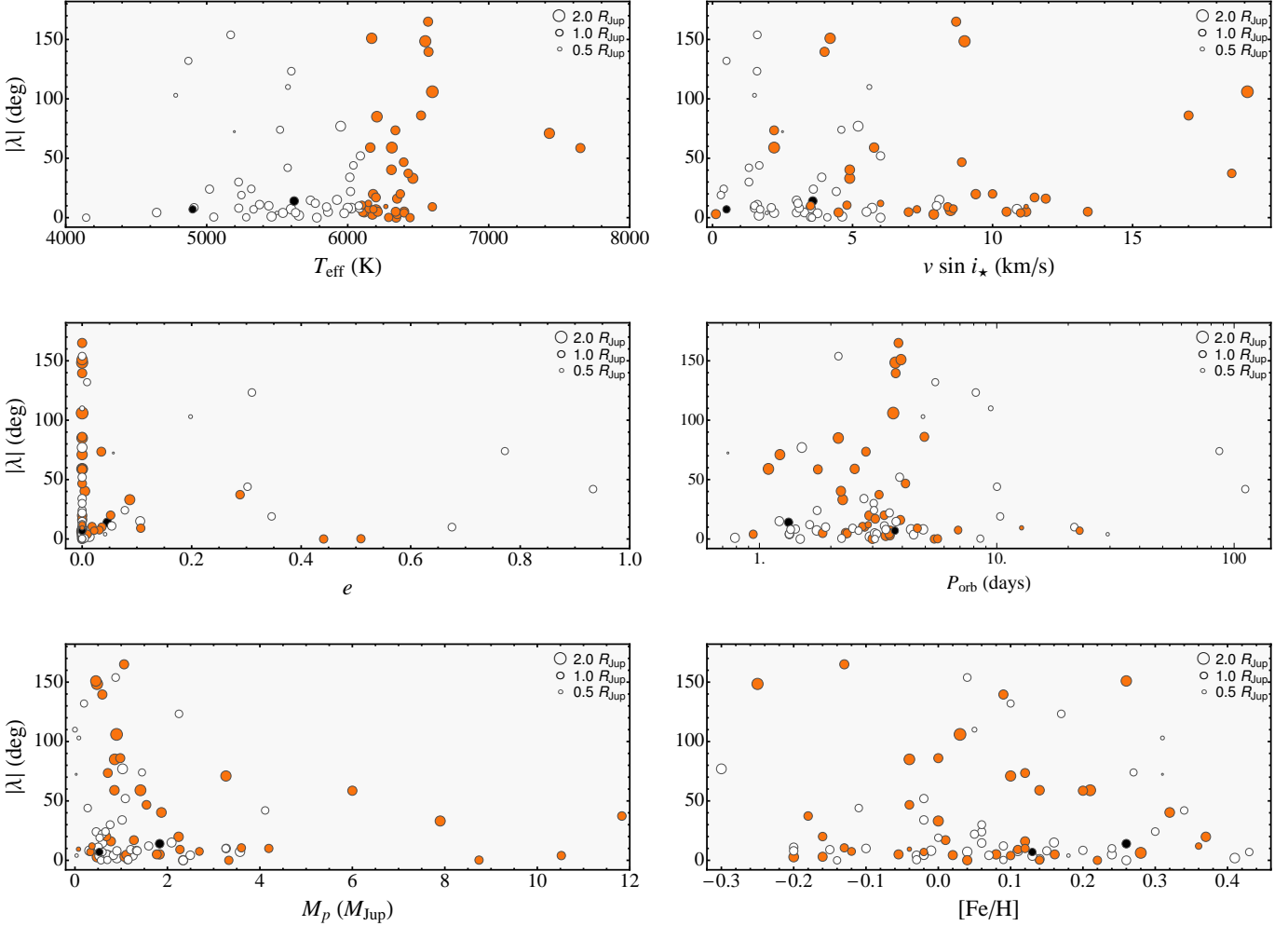


Fig. 12. Sky-projected orbital obliquity as a function of several stellar, orbital and planetary parameters. Orange (white) circles indicate systems in which the parent stars has an effective temperature higher (lower) than 6100 K (Dawson 2014). The size of each circle is proportional to the corresponding planetary radius. The data have been taken from TEPcat (Southworth 2011). The black points indicate the two TEP systems examined in this work, HAT-P-36 and WASP-11/HAT-P-10. The error bars have been suppressed for clarity.

based on data collected with four telescopes during transit events.

By analysing these new photometric and spectroscopic data, we revise the physical parameters of these two systems, finding that previous determinations agree with our more accurate results, within the uncertainties.

Interestingly, we observed anomalies in three photometric transit light curves of HAT-P-36 that, after appropriate modelling, turned out to be compatible with starspot complexes on the photosphere of the star. The main characteristics of the starspots were estimated and compared with those observed in other TEP systems. The HAT-P-36 starspot activity is confirmed by the analysis of the HARPS-N spectra, which give a stellar activity index of $\log R'_{\text{HK}} = -4.65$ dex, and by study of the whole photometric data set collected by the HATNet survey. The frequency analysis of this time-series data revealed a clear modulation in the light curve caused by starspots, allowing us to get an accurate measurement of the rotational period of the star, $P_{\text{rot}} = 15.3 \pm 0.4$ days. A similar study, performed for WASP-11/HAT-P-10 on both the WASP and HATNet sur-

vey light curves, did not highlight any clear photometric modulation.

The RM effect was partially covered in HAT-P-36 (because of bad weather conditions) and wholly observed in WASP-11/HAT-P-10. Thanks to the high-resolution HARPS-N spectra, the sky projection of the orbital obliquity was successfully measured for both the systems, indicating a good spin-orbit alignment. In particular, for the HAT-P-36 system, we were able to also estimate its real obliquity, obtaining $\psi = 25^{+38}_{-25}$ degrees. Our results are thus in agreement with the idea that stars with relatively cool photospheres should have small spin-orbit misalignment angles. However, looking at the entire sample of known TEP systems, for which we have an accurate estimation of λ , there are several exceptions to this scenario. In this context, the case of HAT-P-18 b (Esposito et al. 2014) is emblematic. The collection of more data is thus mandatory for disentangling the issue and understanding whether orbital obliquity really holds imprints of past migration processes that dramatically affected the evolution of giant planets.

Acknowledgements. The HARPS-N instrument has been built by the HARPS-N Consortium, a collaboration between the Geneva

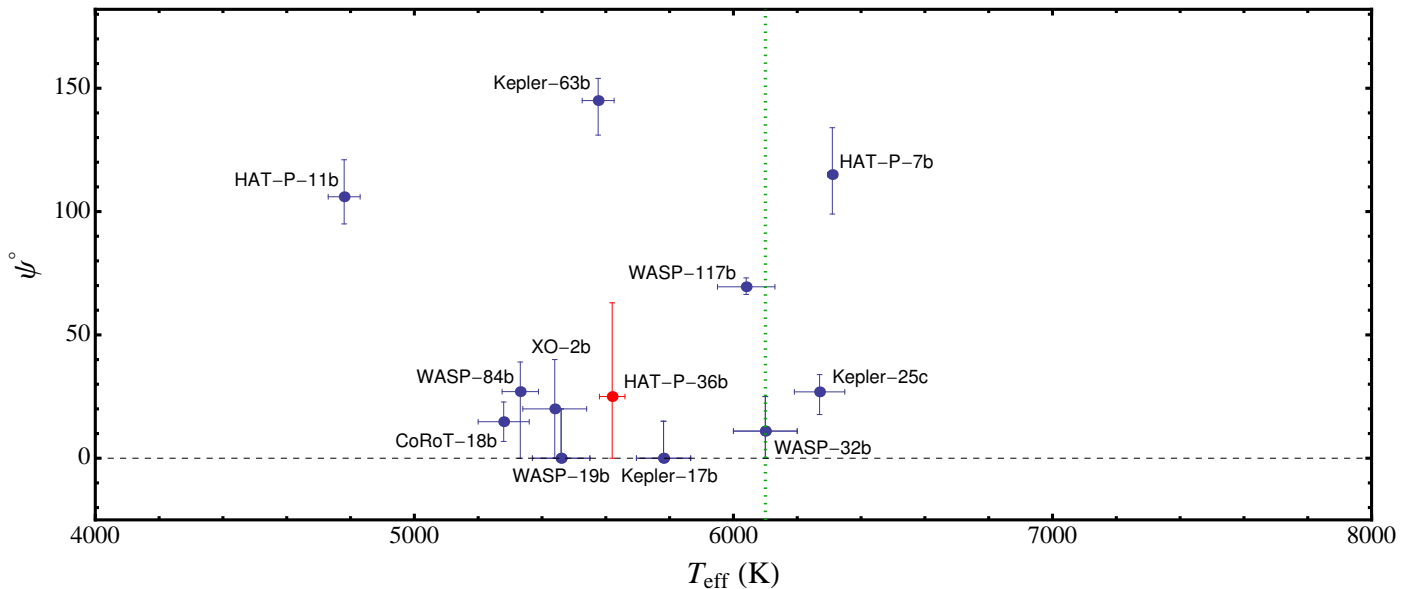


Fig. 14. True orbital obliquity as a function of the effective stellar temperature for 12 TEP systems. Data taken from TEPcat. The red point indicates the location of HAT-P-36 (this work). The temperature range is the same as that in the upper-left panel of Fig. 12. The green-dotted line separates the cool TEP systems from those with $T_{\text{eff}} > 6100$ K (Dawson 2014).

Observatory (PI Institute), the Harvard-Smithsonian Center for Astrophysics, the University of St. Andrews, the University of Edinburgh, the Queen’s University of Belfast, and INAF. Operations at the Calar Alto telescopes are jointly performed by the Max-Planck Institut für Astronomie (MPIA) and the Instituto de Astrofísica de Andalucía (CSIC). The reduced light curves presented in this work will be made available at the CDS (<http://cdsweb.u-strasbg.fr/>). The GAPS project in Italy acknowledges support from INAF through the “Progetti Premiali” funding scheme of the Italian Ministry of Education, University, and Research. We acknowledge the use of the following internet-based resources: the ESO Digitized Sky Survey; the TEPcat catalog; the SIMBAD data base operated at CDS, Strasbourg, France; and the arXiv scientific paper preprint service operated by Cornell University.

References

- Albrecht, S., Winn, J. N., Butler, R. P., et al. 2012a, *ApJ*, 744, 189
 Albrecht, S., Winn, J. N., Johnson, J. A., et al. 2012b, *ApJ*, 757, 18
 Anderson, D. R., Hellier, C., Gillon, M., et al. 2010, *ApJ*, 709, 159
 Anderson, D. R., Triaud, A. H. M. J., Turner, O. D., et al. 2015, *ApJ*, 800, L9
 Bakos, Á. G., Pál, A., Torres, G., et al. 2009, *ApJ*, 696, 1950
 Bakos, Á. G., Hartman, J. D., Torres, G., et al. 2012, *AJ*, 144, 19
 Baranne, A., Queloz, D., Mayor, M., et al. 1996, *A&AS*, 119, 373
 Berdyugina, S. V. 2005, *Living Rev. Sol. Phys.*, 2, 8
 Biazzo, K., D’Orazi, V., Desidera, S., et al. 2012 *MNRAS*, 427, 2905
 Brothwell, R. D., Watson, C. A., Hébrard, G., et al., 2014, *MNRAS*, 440, 3392
 Bryan, M. L., et al., 2012, *ApJ*, 750, 84
 Casagrande, L., Ramirez, I., Meléndez, J., Bessell, M., Asplund, M. 2010, *A&A* 512, A54
 Ciceri, S., Mancini, L., Southworth, J., et al. 2013, *A&A*, 557, A30
 Claret, A. 2004, *A&A*, 424, 919
 Cosentino, R., Lovis, C., Pepe, F., et al. 2012, in *Proc. SPIE*, 8446, 1V
 Covino, E., Esposito, M., Barbieri, M., et al. 2013, *A&A*, 554, A28
 Damasso, M., Biazzo, K., Bonomo, A. S., et al. 2015, to appear in *A&A*, arXiv:1501.01424
 Dawson, R. I. 2014, *ApJ*, 790, 31
 Demarque, P., Woo, J.-H., Kim, Y.-C., Yi, S. K. 2004, *ApJS*, 155, 667
 Desidera, S., Sozzetti, A., Bonomo, A. S., et al. 2013, *A&A*, 554, A29
 Desidera, S., Bonomo, A. S., Claudi, R. U., et al. 2014, *A&A*, 567, L6
 Dotter, A., Chaboyer, B., Jevremović, D., et al. 2008, *ApJS*, 178, 89
 Ehrenreich, D., Désert, J.-M. 2011, *A&A*, 529, A136
 Esposito, M., Covino, E., Mancini, L., et al. 2014, *A&A*, 564, L13
 Hébrard, G., Ehrenreich, D., Bouchy, F., et al. 2011, *A&A*, 527, L11
 Hilditch, R. W. 2001, *An Introduction to Close Binary Stars*, (Cambridge, UK: Cambridge University Press)
 Huitson, C. M., Sing, D. K., Pont, F., et al. 2013, *MNRAS*, 434, 3252
 Knutson, H. A., Charbonneau, D., Noyes, R. W. 2007, *ApJ*, 655, 564
 Knutson, H. A., Howard, A. W., Isaacson, H. 2010, *ApJ*, 720, 1569
 Kovács, G., Bakos, G. Á., Noyes, R. W. 2005, *MNRAS*, 356, 557
 Kuschnig, R., Weiss, W. W., Gruber, R., Bely, P. Y., Jenkner, H. 1997, *A&A*, 328, 544
 Lai, D. 2012, *MNRAS*, 423, 486
 Lendl, M., Triaud, A. H. M. J., Anderson, D. R., et al. 2014, *A&A*, 568, A81
 Lund, M. N., Lundkvist, M., Silva Aguirre, V., et al. 2014, *A&A*, 570, A54
 Maciejewski, G., Puchalski, D., Saral, G., et al. 2013, *IBVS*, 6082, 1
 Mamajek, E. E., Hillenbrand, L. A. 2008, *ApJ*, 687, 1264
 Mancini, L., Southworth, J., Ciceri, S., et al. 2013a, *A&A*, 551, A11
 Mancini, L., Ciceri, S., Chen, G., et al. 2013b, *MNRAS*, 436, 2
 Mancini, L., Southworth, J., Ciceri, S., et al. 2014b, *MNRAS*, 443, 2391
 Mayor, M., Queloz, D. 1995, *Nature*, 378, 355
 Meibom, S., Barnes, S. A., Platais, I., et al. 2015, *Nature*, 517, 589
 Metzger, B. D., Giannios, D., Spiegel, D. S. 2012, *MNRAS*, 425, 2778
 Mohler-Fischer, M., Mancini, L., Hartman, J., et al. 2013, *A&A*, 558, A55
 Mordasini, C., Mollière, P., Dittkrist, K.-M., et al. 2014, to appear in *IJA*, arXiv:1406.5604
 Noyes, R. W., Hartmann, L. W., Baliunas, et al. 1984, *ApJ*, 279, 763
 Ogilvie, G., & Lin, D. 2007, *ApJ*, 661, 1180
 Pepe, F., Mayor, M., Galland, F., et al. 2002, *A&A*, 388, 632
 Pietrinferni, A., Cassisi, S., Salaris, M., Castelli, F. 2004, *ApJ*, 612, 168
 Rabus, M., Alonso, R., Belmonte, J. A., et al. 2009, *A&A*, 494, 391
 Rogers, T. M., Lin, D. N. C. 2013, *ApJ*, 769, 10
 Sada, P. V., Deming, D., Jennings, D. E., et al. 2012, *PASP*, 124, 212
 Sanchis-Ojeda, R., Winn, J. N., Holman, M. J. 2011, *ApJ*, 733, 127
 Sanchis-Ojeda, R., Winn, J. N., Marcy, G. W. 2013, *ApJ*, 775, 54
 Seager, S., Mallén-Ornelas, G. 2003, *ApJ*, 585, 1038
 Silva, A. V. R. 2003, *ApJ*, 585, L147
 Silva-Valio, A., Lanza, A. F., Alonso, R., Barge, P. 2010, *A&A*, 510, A25
 Sing, D. K., Pont, F., Aigrain, S., et al. 2011, *MNRAS*, 416, 1443
 Sneden, C. 1973, *ApJ*, 184, 839
 Southworth, J. 2008, *MNRAS*, 386, 1644

- Southworth, J. 2011, MNRAS, 417, 2166
Southworth, J. 2012, MNRAS, 426, 1291
Southworth, J. 2013, A&A, 557, 119
Southworth, J., Wheatley, P. J., Sams, G. 2007, MNRAS, 379, L11
Southworth, J., Hinse, T. C., Burgdorf, M., et al., 2014, MNRAS, 444, 776
Sozzetti, A., Torres, G., Charbonneau, D., et al. 2007, ApJ, 664, 1190
Strassmeier, K. G. 2009, Astron. Astrophys. Rev., 17, 251
Tregloan-Reed, J., Southworth, J., Tappert, C. 2013, MNRAS, 428, 3671
Tregloan-Reed, J., Southworth, J., Burgdorf, M. 2015, MNRAS in press, [arXiv:1503.09184](https://arxiv.org/abs/1503.09184)
Triaud, A. H. M. J., Collier Cameron, A., Queloz, D., et al. 2010, A&A, 524, A25
Valsecchi, F., Rasio, F. A. 2014, ApJ, 786, 102
VandenBerg, D. A., Bergbusch, P. A., Dowler, P. D. 2006, ApJS, 162, 375
Vaniček, P. 1971, Ap&SS, 12, 10
Wang, X., Gu, S., Collier Cameron, A., et al. 2014, AJ, 147, 92
West, R. G., Collier Cameron, A., Hebb, L., et al. 2009, A&A, 502, 395
Winn, J. N., Holman, M. J., Henry, G. W., et al. 2007, AJ, 133, 1828
Winn, J. N., Fabrycky, D., Albrecht, S., Johnson, J. A. 2010, ApJ, 718, L145
Xue, Y., Suto, Y., Taruya, A., et al. 2014, ApJ, 784, 66

Appendix A: Supplementary tables

The tables in this Appendix contain the detailed results of the predictions of different sets of stellar evolutionary models for the HAT-P-36 and WASP-11/HAT-P-10 planetary systems. The final values of the physical parameters for each of the two systems (see Tables 8 and 9), are calculated by taking the unweighted mean of the five estimates of the different sets of model predictions (see Sect 5).

Table A.1. Derived physical properties of the HAT-P-36 system based on the prediction of different theoretical models.

	(Claret models)	(Y ² models)	(BaSTI models)	(VRSS models)	(DSEP models)
K_b (km s ⁻¹)	196.19 ± 4.95	196.09 ± 1.79	193.00 ± 1.62	193.00 ± 2.76	196.17 ± 0.32
M_* (M_\odot)	1.0503 ± 0.0840	1.0486 ± 0.0287	1.0000 ± 0.0259	1.0000 ± 0.0426	1.0500 ± 0.0045
R_* (R_\odot)	1.048 ± 0.029	1.047 ± 0.012	1.031 ± 0.013	1.031 ± 0.018	1.048 ± 0.010
log g_* (cgs)	4.4192 ± 0.0132	4.4190 ± 0.0100	4.4121 ± 0.0092	4.4121 ± 0.0109	4.4192 ± 0.0085
M_p (M_{Jup})	1.877 ± 0.130	1.875 ± 0.088	1.816 ± 0.087	1.816 ± 0.095	1.876 ± 0.079
R_p (R_{Jup})	1.313 ± 0.038	1.312 ± 0.020	1.291 ± 0.021	1.291 ± 0.025	1.313 ± 0.018
ρ_p (ρ_{Jup})	0.776 ± 0.049	0.776 ± 0.046	0.789 ± 0.047	0.789 ± 0.048	0.776 ± 0.047
Θ	0.0654 ± 0.0033	0.0654 ± 0.0030	0.0665 ± 0.0030	0.0665 ± 0.0032	0.0654 ± 0.0030
a (AU)	0.024040 ± 0.000605	0.024028 ± 0.000219	0.023651 ± 0.000198	0.023651 ± 0.000338	0.024038 ± 0.000036
Age (Gyr)	4.3 ^{+2.4} _{-1.4}	4.0 ^{+1.1} _{-0.8}	7.6 ^{+4.3} _{-1.9}	5.0 ^{+1.5} _{-2.0}	1.7 ^{+7.5} _{-0.1}

Notes. In each case $g_p = 27.0 \pm 1.4 \text{ m s}^{-2}$, $\rho_* = 0.913 \pm 0.027 \rho_\odot$ and $T_{\text{eq}} = 1788 \pm 15 \text{ K}$.

Table A.2. Derived physical properties of the WASP-11/HAT-P-10 system based on the prediction of different theoretical models.

	(Claret models)	(Y ² models)	(BaSTI models)	(VRSS models)	(DSEP models)
K_b (km s ⁻¹)	129.9 ± 3.2	127.7 ± 2.0	127.5 ± 1.9	127.5 ± 2.3	128.4 ± 2.1
M_* (M_\odot)	0.846 ± 0.063	0.804 ± 0.039	0.800 ± 0.036	0.800 ± 0.043	0.818 ± 0.038
R_* (R_\odot)	0.785 ± 0.023	0.772 ± 0.013	0.771 ± 0.015	0.771 ± 0.014	0.777 ± 0.012
log g_* (cgs)	4.576 ± 0.016	4.569 ± 0.016	4.568 ± 0.015	4.568 ± 0.018	4.571 ± 0.018
M_p (M_{Jup})	0.508 ± 0.028	0.492 ± 0.020	0.490 ± 0.019	0.490 ± 0.024	0.497 ± 0.023
R_p (R_{Jup})	1.006 ± 0.031	0.989 ± 0.019	0.987 ± 0.020	0.987 ± 0.023	0.995 ± 0.022
ρ_p (ρ_{Jup})	0.467 ± 0.028	0.475 ± 0.025	0.476 ± 0.026	0.476 ± 0.027	0.472 ± 0.026
Θ	0.0531 ± 0.0021	0.0540 ± 0.0016	0.0541 ± 0.0017	0.0541 ± 0.0019	0.0537 ± 0.0019
a (AU)	0.04447 ± 0.00111	0.04373 ± 0.00069	0.04365 ± 0.00065	0.04365 ± 0.00080	0.04398 ± 0.00070
Age (Gyr)	5.7 ^{+5.8} _{-4.8}	8.9 ^{+3.9} _{-3.9}	6.2 ^{+2.7} _{-2.5}

Notes. In each case $g_p = 12.45 \pm 0.50 \text{ m s}^{-2}$, $\rho_* = 1.748 \pm 0.074 \rho_\odot$ and $T_{\text{eq}} = 992 \pm 14 \text{ K}$. We were not able to constrain a reasonable value for the age of the WASP-11/HAT-P-10 system by using the BaSTI and VRSS models, because the evolution of a star of the mass of WASP-11 is small for times shorter than the age of the Galaxy.